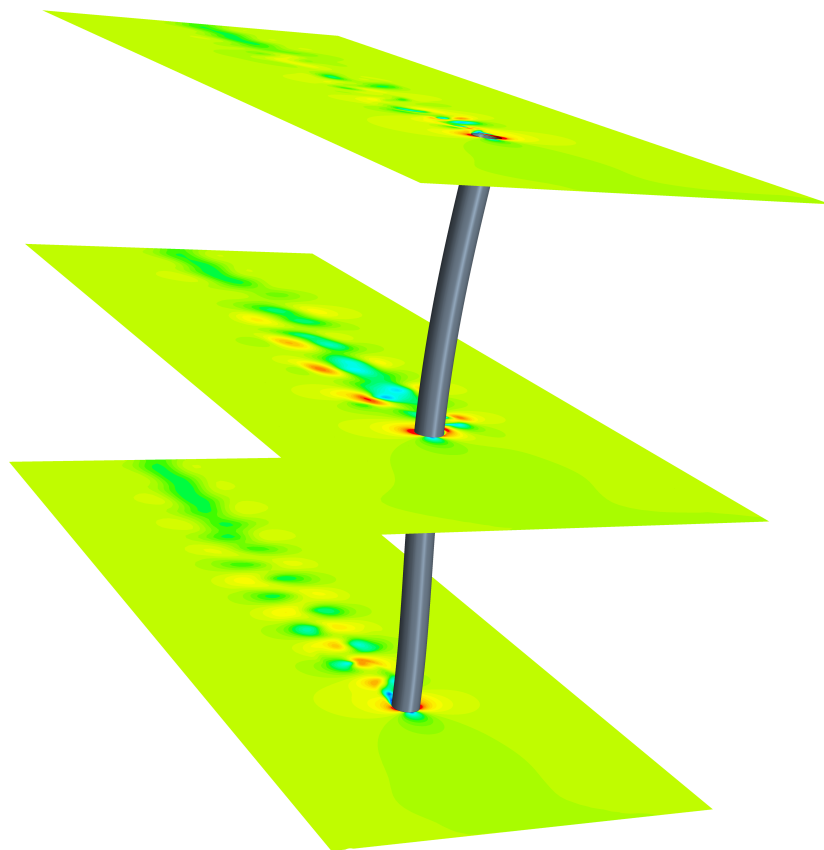


# CHALMERS



## Analysis of Vortex-Induced Vibrations of Risers

*Master's thesis in Applied Mechanics*

ANTON GUSTAFSSON

Department of Applied Mechanics  
*Division of Material and Computational Mechanics*  
CHALMERS UNIVERSITY OF TECHNOLOGY  
Gothenburg, Sweden 2012  
Master's thesis 2012:60



MASTER'S THESIS IN APPLIED MECHANICS

# Analysis of Vortex-Induced Vibrations of Risers

ANTON GUSTAFSSON

Department of Applied Mechanics  
*Division of Material and Computational Mechanics*  
CHALMERS UNIVERSITY OF TECHNOLOGY  
Gothenburg, Sweden 2012

Analysis of Vortex-Induced Vibrations of Risers  
ANTON GUSTAFSSON

© ANTON GUSTAFSSON, 2012

Master's thesis 2012:60  
ISSN 1652-8557  
Department of Applied Mechanics  
Division of Material and Computational Mechanics  
Chalmers University of Technology  
SE-412 96 Gothenburg  
Sweden  
Telephone: +46 (0)31-772 1000

Cover:  
Velocity field and deformation of a short riser in VIV flow

Chalmers Reproservice  
Gothenburg, Sweden 2012

Analysis of Vortex-Induced Vibrations of Risers  
Master's thesis in Applied Mechanics  
ANTON GUSTAFSSON  
Department of Applied Mechanics  
Division of Material and Computational Mechanics  
Chalmers University of Technology

## ABSTRACT

Fluid-structure interaction (FSI) is a challenging field in engineering analysis and many aspects must be taken into account. Large deformations are particular critical in FSI problems and one component related to the off-shore industry that can be subjected to large deformations is the riser. The large deformations of risers are caused by Vortex induced vibration (VIV) and the purpose of this thesis is to develop a method to simulate riser VIV. Only a short section of the riser is evaluated and the model is based on experience from three preparatory studies.

Simulating riser VIV with FSI is very time-consuming and strongly mesh dependent. Different mesh qualities and turbulence models have been evaluated to find an economic model. Many parameters have been found to be important to obtain a stable FSI coupling and an iterative FSI approach with small time steps are necessary to apply in order to obtain a stable solution. The fluid mesh used for the fully coupled analysis is very coarse and the results should be verified before further evaluations are made.

Keywords: Fluid-Structure Interaction; Vortex-Induced Vibration; Riser

## ACKNOWLEDGEMENTS

The present work has been conducted at FS Dynamics and I would like to thank FS Dynamics for making it possible to perform this master thesis. The thesis has been performed in collaboration with FMC Technologies and data provided from FMC has facilitated the study. I would especially like to thank my Supervisors Fredrik Karström and Ulf Engdär for support and guidance. I would also thank Christoffer Cromik, Fredrik Carlson and Ola Dahlin for their help and valuable advice. Finally, I also would like to thank my examiner at Chalmers University of Technology, Prof. Magnus Ekh for his help during this thesis.



## Abbreviations

2D	-	Two-Dimensional
3D	-	Three-Dimensional
APG	-	Adverse Pressure Gradient
CF	-	Cross-Flow
CFD	-	Computational Fluid Dynamics
FEA	-	Finite Element Analysis
FEM	-	Finite Element Method
FSI	-	Fluid-Structure Interaction
Hz	-	Hertz
$kSm^3/day$	-	Thousand standard cubic meters per day
MIT	-	Massachusetts Institute of Technology
$MSm^3/day$	-	Million standard cubic meters per day
Pa	-	Pascal
RANS	-	Reynolds Average Navier Stoke
SST	-	Shear Stress Transport
VIV	-	Vortex Induced Vibrations

## Greek letters

$\Gamma$	-	Fluid-Structure interface
$\nu_s$	-	Poisson's ratio
$\nu_f$	-	Kinematic viscosity
$\rho$	-	Density

## Roman letters

A	-	Response amplitude
$C_D$	-	Drag coefficient
$C_L$	-	Lift coefficient
D	-	Diameter
E	-	Young's modulus
$F_D$	-	Drag force
$F_L$	-	Lift force
$f_s$	-	Shedding frequency
$f_o$	-	Natural frequency
L	-	Length
m	-	Meter
$m_f$	-	Fluid mass
$m_s$	-	Structural mass
N	-	Newton
r	-	radius
s	-	Second
U	-	Velocity

## Dimensionless quantities

$C_a$	-	Added mass coefficient
$m^*$	-	Mass ratio
Re	-	Reynolds number
St	-	Strouhal number
$V_r$	-	Reduced velocity
$y^+$	-	Dimensionless wall distance

## Subscripts

$f$	-	Fluid
$s$	-	Structure





# Contents

<b>1</b>	<b>Introduction</b>	<b>1</b>
1.1	Background . . . . .	1
1.1.1	Gjøa field . . . . .	2
1.2	Purpose . . . . .	2
1.3	Previous work . . . . .	2
<b>2</b>	<b>Theory</b>	<b>4</b>
2.1	Coupled systems . . . . .	4
2.1.1	Monolithic approach . . . . .	5
2.1.2	Partitioned approach . . . . .	5
2.1.3	Mesh motion . . . . .	6
2.2	Fluid theory . . . . .	7
2.2.1	Flow around circular cylinders . . . . .	7
2.2.2	Boundary layers . . . . .	7
2.2.3	Turbulence . . . . .	9
2.2.4	Introduction to VIV . . . . .	10
2.2.5	Vortex shedding . . . . .	11
2.2.6	Lock in . . . . .	12
2.2.7	A/D . . . . .	13
2.2.8	Added mass . . . . .	14
2.2.9	Drag- and lift coefficient . . . . .	14
2.3	Structural theory . . . . .	15
2.3.1	Morison equation . . . . .	15
2.3.2	Mode-Superposition of an undamped structure . . . . .	15
<b>3</b>	<b>Benchmark</b>	<b>17</b>
3.1	Software . . . . .	17
3.1.1	Abaqus 6.12 . . . . .	17
3.1.2	AcuSolve 1.8b . . . . .	17
3.1.3	STAR-CCM+ 7.04.006 . . . . .	17
3.2	Method benchmark . . . . .	17
3.2.1	Geometry . . . . .	18
3.2.2	Structural mesh . . . . .	18
3.2.3	Material properties . . . . .	18
3.2.4	STAR-CCM+ . . . . .	19
3.2.5	AcuSolve . . . . .	21
3.2.6	Boundary condition . . . . .	22
3.3	Results benchmark . . . . .	22
3.3.1	Developing flow . . . . .	23
3.3.2	Fully developed flow . . . . .	24
3.4	Discussion benchmark . . . . .	28
<b>4</b>	<b>Riser analysis</b>	<b>29</b>
4.1	Method preparation work . . . . .	29
4.1.1	Geometry . . . . .	29
4.1.2	Modelling of riser . . . . .	30
4.1.3	Boundary conditions . . . . .	30
4.1.4	Currents at Gjøa field . . . . .	30

4.1.5	Frequency analysis . . . . .	31
4.1.6	VIV analysis . . . . .	31
4.2	Results riser analysis . . . . .	31
4.3	Discussion riser analysis . . . . .	34
<b>5</b>	<b>CFD on short riser</b>	<b>36</b>
5.1	Method CFD on short riser . . . . .	36
5.1.1	Geometry and mesh . . . . .	36
5.2	Results CFD on short riser . . . . .	38
5.2.1	Lift coefficient . . . . .	39
5.2.2	Drag coefficient . . . . .	41
5.2.3	Near wall treatment . . . . .	43
5.3	Discussion CFD on short riser . . . . .	44
<b>6</b>	<b>Fluid-Structure Interaction on riser</b>	<b>46</b>
6.1	Method Fluid-Structure Interaction on short riser . . . . .	46
6.1.1	Geometry and mesh . . . . .	46
6.2	Results Fluid-Structure Interaction on short riser . . . . .	48
6.3	Discussion Fluid-Structure Interaction on Riser . . . . .	52
<b>7</b>	<b>Concluding remarks</b>	<b>53</b>



# 1 Introduction

## 1.1 Background

The offshore industry is a huge industry that is very important from an economical perspective. It is very important that the offshore platforms produce as much as possible and unexpected stoppages are very expensive. More important, is to ensure prevailing environmental and avoid disasters as in the Gulf of Mexico 2010 [1]. Failures in drilling and pumping equipment can be fateful or at least expensive. One of the most critical components concerning offshore industry is the riser, which connect the platform with the well at the sea bed, see Figure 1. The riser is used both for drilling and environmental protection and it is subjected to large forces, due to waves and underwater currents. The design and operation of risers are complex processes, and requirements for safety and reliability mean that an extensive amount of engineering analysis is required. Production in deep sea fields gives rise to even higher loads and stresses and further engineering analysis becomes more and more important.

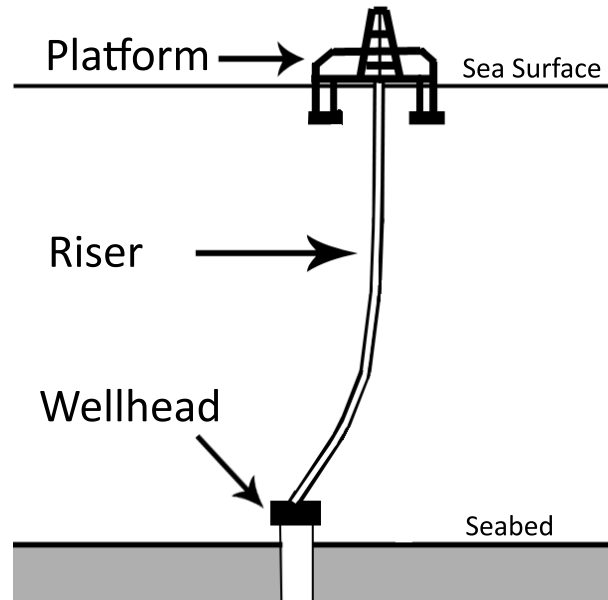


Figure 1: Principle sketch of a riser system

Numerical methods play an important role in predicting hydrodynamic motion and forces on the riser. The riser motion is initiated by VIV (Vortex Induced Vibrations) and if the riser motion is equal to one of the natural frequencies the fatigue life decreases rapidly. Using empirical methods are today the leading approach for simulating VIV of risers, but more general methods based on Fluid-Structure Interaction (FSI) become more and more interesting, as the computational resources improve. Prediction of riser VIV are complex and a combination of several engineering problems must be considered. Unsteady conditions that occur in the ocean makes it impossible to get totally correct predictions of the riser motion. The flow around the riser is affected by vortices, which are complex and fully 3D in nature. As the current change in direction and magnitude along the riser and over time, the flow field around the riser also changes. The motion of the riser is large and strongly affects the flow field, and therefore need to be fully coupled with the fluid motion, Two-way FSI must be implemented, see Section 2.1. The platform at deep sea fields is floating and the vessel motion has also some influence on the riser motion. Suppression devices, such as strakes and fairings are used to eliminate or reduce VIV response and prevent fatigue damage.

Risers are long and flexible structures and the critical ratio  $L/D$  tends to be very large. This is particularly a problem in deep ocean areas, as in the Gulf of Mexico, where the world's deepest platform the Perdido spar is floating on 2,438 meters deep water [2]. Even in shallower water, as the case is at the North Sea the ratio  $L/D$  is large, which makes it difficult to perform CFD simulations since the required number of elements in the mesh tends to be enormous. One oilfield in the Norwegian section of the North Sea is the Gjøa field, see Section 1.1.1, which has been used as reference object in this thesis.

The riser investigated in this thesis is a top tensioned workover riser that is used in the installation procedure. The workover riser is a flexible riser and the use of flexible risers have increased significantly in recent years since the drilling depths becomes deeper and deeper. The drilling depth tends to increase as long as the price on oil is high and drilling techniques are improved. The risers at deep sea oilfields are long and flexible and the eigenfrequencies are low. Low-order eigenmodes are, therefore, expected to be excited even in shallow current. Another trend in the offshore industry is to drill in regions with extreme weather conditions and high currents. Extreme conditions are critical since higher eigenmodes can be excited which results in reduced fatigue life.

### 1.1.1 Gjøa field

The reference object in this thesis is a riser in the Gjøa oil- and gas field. The field is located on the Norwegian section of the North Sea 130 km northwest of Bergen at a water depth of 380m. The Gjøa field was named after Roald Amundsens polar exploration vessel and was discovered in 1989. The reserves are estimated to be 82 million barrels of oil and condensate and 40 billion cubic meters of gas. The development of Gjøas floating platform started in 2007 and the production in 2010. The export capacity for oil is  $13.8 \text{ kSm}^3/\text{day}$  and  $17 \text{ MSm}^3/\text{day}$  for gas. The Gjøa platform is the first floating platform to receive electrical power from the mainland. This means a reduction in emissions to the environment of 250,000 tonnes of carbon dioxide per year [3]. Together with the neighboring field Vega, the fields are the biggest development projects being carried out in the North Sea at present. The fields are, based on current technology, estimated to produce oil and gas for roughly 15 more years. The platform is designed to have a lifetime of at least 30 years, to secure production if the technology improves so that more oil and gas can be extracted.

## 1.2 Purpose

FS Dynamics has no experience of VIV analysis of risers and FMC Technologies desire a method to solve these kinds of problems with Fluid-Structure Interaction. The purpose of this thesis is to study VIV of risers and develop a method to simulate a full-scale riser exposed to VIV. The method should be based on fully 3D CFD simulations. The study includes an evaluation of AcuSolve and STAR-CCM+ ability to solve intractable FSI problems.

## 1.3 Previous work

The problems with VIV on risers have been known for a long time and countless of research has been performed in the field. Large resources have been spent to predict and understand VIV. The first studies regarding vortex shedding and VIV was connected to experiments on cylinders submerged in water. The result from those studies gives understanding of how the fluid and structural properties affect the flow and vice versa [4] and [5]. VIV can be predicted by both empirical models and FSI simulations. Empirical models for VIV prediction of risers have been

used since the early eighties and in later years, also CFD simulations have been performed.

### Empirical models

One of the most important milestones of VIV research was presented in the late 80's by Professor J. Kim Vandiver and his research group at MIT. The research program was called SHEAR which resulted in the software SHEAR7. SHEAR7 is based on empirical models and use mode-superposition to calculate the structural motion of the riser. The program is simple and fast to run and it is today, after several updates, possible to simulate cylinders without uniform cross section, strakes and varying currents. Other popular software for VIV analysis on slender marine structures are *VIVANA*, *VIVA* and *ABAVIV*. *VIVANA* and *VIVA* are together with SHEAR7 so-called frequency domain models, whereas *ABAVIV* is a so called time domain model. The empirical models usually show good agreement with experiments and they are still the leading method in practical engineering on long flexible systems, such as risers. The main limitation with empirical models based on frequency domains, are that they cannot handle non-linearities.

### CFD

In later years, several CFD studies on fixed and vibrating cylinders have been performed with valuable results. Accurate results have been shown for analysis on very short risers by using very fine mesh resolution. The limitation with CFD for this application is the computational time. Hence, completed and accurate CFD-simulations on risers are not practicable. In fact, it exists a couple of approaches that can solve VIV problems on long flexible risers with more or less accurate results using CFD. These methods are based on very course 3D meshes [6] or on a method called strip theory [7] and [8]. The strip theory assumes that the fluid flow solution can be obtained on a series of two dimensional planes along the riser axis. These strips are connected with a structural model of the riser to obtain a prediction of the fluid-structure response. This idea results in a number of 2D problems instead of a full 3D problem. Strip theory has become quite popular, but it has some serious shortcomings. Flow around bluff bodies is inherently three dimensional so that although the 2D solutions predict the motion well in some circumstances, they may not be good approximations for the full model. Risers exposed to VIV are inclined to the flow over much of their length and these effects are not captured by CFD simulations. The use of the strip theory also implies that some interpolation method is assumed to estimate the forces between the strips and there is no general rule on how to make such interpolations.

## 2 Theory

FSI problems can be very different in nature and they can be solved in a couple of various manners. Depending on expected deformations, stability requirements and time limit, an appropriate approach is decided. To solve FSI problems where VIV occur, a theoretical understanding of both the structural and the fluid behavior, as well as the VIV phenomena itself, is necessary. This theory chapter are divided into three parts and start with governing theory of FSI followed by fluid and structural theory.

### 2.1 Coupled systems

In a coupled system, two or more physical systems interact. One example of a coupled system is FSI, where a fluid and a structure are the physical systems. The structure can be movable and/or deformable and the fluid flow can be internal and/or external. Forces due to a moving fluid are applied as pressure on the structure, which then will be deformed. FSI problems can be divided into two groups, One-way FSI and Two-way FSI. If no feedback from the structure to the fluid is used, the system is called one-way FSI. If ongoing feedback between the systems is used, it is called Two-way FSI. A couple of different methods are available for solving FSI problems. The two most common solution methods are a partitioned approach and a monolithic approach.

#### One-way FSI

One-way FSI is a weak coupling between a fluid and a structure. It is applicable when the structural motions and deformations are small and not influence the fluid motion to a large extent. One example is when a fluid heat or cool a stiff and supported structure, which produces thermal stress loads and deformations in the structure. The deformation of the structure is so small that the flow field not will change. The other possible application of One-way FSI is when the fluid motion do not affect the motion of the structure. This is the case when a piston moves in a combustion chamber [9].

The general procedure of One-way FSI for a deformable structure starts with a CFD simulation to compute a pressure acting on the structure. The next step is to run a structural simulation with the calculated pressure as load and then determine the structural deformation and the stresses.

#### Two-way FSI

Two-way FSI should be used when the interaction between the fluid and the structure is significant. One example is when the structural deformations are large and the new shape of the structure and its velocity affect the flow field in a way that will change the loads on the structure. For applications exposed to VIV, Two-way FSI is the only possible approach. Two-way FSI is a transient problem and information about pressure, shear stresses and deformation are continuously transferred between the fields. All FSI approaches described in this thesis utilize a Two-way coupling.

Independent of solution method, two general conditions must be fulfilled. The interface conditions of displacement continuity (motion transfer), Equation 1, and traction equilibrium (momentum transfer), Equation 2 must be satisfied along the fluid-structure boundary [10].

$$\mathbf{d}_f = \mathbf{d}_s \quad \text{on } \Gamma_{fsi} \quad (1)$$

$$\mathbf{P}_f = \mathbf{P}_s \quad \text{on } \Gamma_{fsi} \quad (2)$$



### 2.1.1 Monolithic approach

A monolithic approach (also called direct approach) solves both the structural and fluid equations simultaneously in one single matrix system. The matrix system tends to be very large for large models and the computational time increases a lot since the methods requires a lot of memory. Improvements in the solution method has been performed to reduce the computational time, but the approach is still impractical [11] and [12]. On the other hand, monolithic solvers as ADINA and COMSOL appear to be unconditionally stable (possible to use larger time steps) as compared to a partitioned scheme.

### 2.1.2 Partitioned approach

Partitioned approaches are rather popular for simulation of FSI problems, and the main reason to this is that it allows using specifically designed codes on the different fields. For large systems, this approach benefits in terms of efficiency, compared to monolithic solvers since smaller and better conditioned subsystems are solved instead of one large problem.

Partitioned coupling schemes can either be loosely or strongly coupled. Both methods can be applied on FSI-problems and which method that is preferable depend on stability requirement. The stability of the FSI-coupling has been investigated in [13]. The solution method used for each subsystem has nothing to with the coupling method. Implicit solvers for both fluid and structural fields can be coupled in an explicit manner.

A typical partitioned method are based on the following sequential process [12]:

1. Transfer the motion of the structural boundary to the fluid,
2. Update the position of the moving fluid mesh,
3. Advance the fluid system in time and compute the new pressure,
4. Convert the new fluid pressure into a structural load,
5. Advance the structural system in time under the fluid-induced load.

### Loose coupling

In a loosely coupled scheme, each field is solved only once per time step and is thus favorably in terms of efficiency. The most usual algorithm for loosely coupled system is to solve the system in a sequentially staggered manner, but both a Gauss-Seidel method and a Jacobi method are applicable. Previous studies have observed that a loosely coupling between fluid and structural fields for incompressible flow and slender structures using sequentially staggered schemes yields unstable computations. The main reason for the instability depends on the density ratio of fluid and structure and the geometry of the domain [14] and [15]. The instability is inherent in the scheme itself and occurs due to lack of energy equilibrium, which increases the total energy in the system. The increase of energy leads to high under- or over-prediction of pressure on the interface surface. The fluid forces depend upon predicted structural interface displacements rather than the correct ones and thus contain a portion of incorrect coupling forces. Even a small error of the interface displacement gives a large error in the fluid pressure. The error can be originated from the extra mass from the fluid that contributes to the structural mass. This is called artificial added mass effect [14]. Reducing the time step has not a positive effect on the stability, rather opposite effect. The loosely coupling is only recommended for weak interactions such as aero elastic applications or where the effect of the structure on the fluid is much larger than the effect of the fluid on the structure.

A number of explicit coupling methods have been developed to enhance the coupling stability such as Generalized Sequential Staggered (GSS) [16] and Modified Combined-Interface Boundary Conditions (M-CIBC) [17]. A variety of structural predictors and force correctors (artificial added mass) are applied at each time step and give more stable solutions but it is in many cases not sufficient.

### Strong coupling

Strongly coupled systems, referred as Multi iterative couplings in AcuSolve [10], utilize an iteration method to get convergence before further time-stepping. Data will be transferred between the fluid and structural solver until the solution converges within each time step. The strong coupling is much more stable than the explicit coupling, but also more time consuming. The iteratively staggered partitioned scheme is energy conservative at the coupling interface and hence more stable.

#### 2.1.3 Mesh motion

For both the fluid motion and the structural motion, an appropriate kinematic description of the continuum must be chosen. The governing equations of motion are generally described from either an Eulerian or a Lagrangian point of view. Usually, Eulerian equations are used in fluid mechanics and Lagrangian equations are used in structural mechanics.

### Lagrangian formulation

Each node of the computational mesh follows the associated material point during the motion in the Lagrangian formulation. The Lagrangian description makes it possible to track back loading history of the material, and therefore, suitable when working with material with history dependent behavior. Tracking of free surfaces and interfaces between different materials is easily performed in the Lagrangian formulation and the results, in form of material displacements are accurate. The main drawback of this formulation is when the continuum undergoes large deformations. Then, the mesh will be distorted which might cause problems with accuracy and stability. Remeshing is possible to perform, but that is computationally expensive, in particular for a 3D case.

### Eulerian formulation

Eulerian algorithms are widely used in fluid dynamics and in this formulation, the computational mesh is fixed and the continuum moves with respect to the grid. In the Eulerian description, large distortions in the continuum motion can be handled with relative ease, but generally at the expense of precise interface definition and the resolution of flow details.

### ALE formulation

When coming to multiphysics problems such as FSI-problems, both these classical approaches have their drawbacks. A new method based on a combination of the Eulerian and Lagrangian formulation has been developed, called Arbitrary Lagrangian-Eulerian formulation (ALE). The ALE description offers freedom in moving the computational mesh and large distortions of the continuum can be handled with high resolution and accuracy. Nodes either follow the continuum as in the Lagrangian description, are fixed as in Eulerian description or move arbitrary to get continuously rezoning capability. The result is a computational mesh that can avoid large mesh distortion with good resolution. When choosing the ALE method to describe the motion of the

continuum new formulations of the governing equations must be introduced.

The conservation equations for mass, momentum and energy expressed in ALE formulation read:

$$\text{Mass :} \quad \left. \frac{\partial \rho}{\partial t} \right|_{\mathbf{x}} + \mathbf{c} \cdot \nabla \rho = -\rho \nabla \cdot \mathbf{v} \quad (3)$$

$$\text{Momentum :} \quad \rho \left( \left. \frac{\partial \mathbf{v}}{\partial t} \right|_{\mathbf{x}} + (\mathbf{c} \cdot \nabla) \mathbf{v} \right) = \nabla \cdot \boldsymbol{\sigma} + \rho \mathbf{b} \quad (4)$$

$$\text{Total energy :} \quad \rho \left( \left. \frac{\partial E}{\partial t} \right|_{\mathbf{x}} + \mathbf{c} \cdot \nabla E \right) = \nabla \cdot (\boldsymbol{\sigma} \cdot \mathbf{v}) + \mathbf{v} \cdot \rho \mathbf{b} \quad (5)$$

For further details see [18] and [19].

### Morphing

Morphing is another method to move the grid in junction with the structural motion in FSI problems. Morphing is sometimes referred as ALE, but ALE is associated with finite element analysis (FEA) rather than finite volume analysis (FVA). STAR-CCM+ is based on FVA and use morphing for grid updating. The mesh morpher uses control points and their associated displacements to generate an interpolation field throughout the region, which can then be used to displace the actual vertices of the mesh. Each control point has an associated distance vector which specifies the displacement of the point within a single time-step. A reasonable qualitative fluid grid is maintained, by moving these vertices in the fluid mesh. For further details see [9]

## 2.2 Fluid theory

The flow is fully described by the Navier-Stokes equations, see Equation 6 and the continuity equation, see Equation 7.

$$\frac{\partial \rho}{\partial t} + \frac{\partial(\rho v_i)}{\partial x_i} = 0 \quad (6)$$

$$\rho \frac{\partial v_i}{\partial t} + \rho \frac{\partial v_i v_j}{\partial x_j} = \frac{\partial p}{\partial x_i} + \mu \frac{\partial^2 v_i}{\partial x_j \partial x_j} \quad (7)$$

### 2.2.1 Flow around circular cylinders

The riser is often modelled as a cylinder and this section describes the physics of flow around circular cylinders. Flow around circular cylinders is well documented for both fixed and vibrating cylinders. The flow is characterized by the Reynolds number, defined as:

$$Re = \frac{UD}{\nu_f} \quad (8)$$

Where  $U$  is the free-stream velocity,  $D$  the cylinder diameter and  $\nu_f$  the kinematic viscosity.

### 2.2.2 Boundary layers

One important aspect to get good prediction of the forces acting on the riser is related to correct modelling of the physics in the boundary layers. In the boundary layer, energy dissipates due to viscous drag and the flow remains without sufficient kinetic energy and separation takes place. Correct prediction of the separation point, which depends both on surface roughness and Reynolds number, is a challenging difficulty. Separation take place when the adverse pressure

gradient (APG) becomes critical [20].

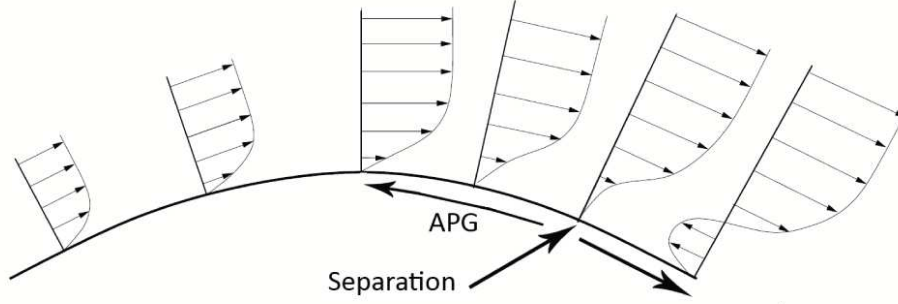


Figure 2: Velocity profiles for flow over a curved surface [20]

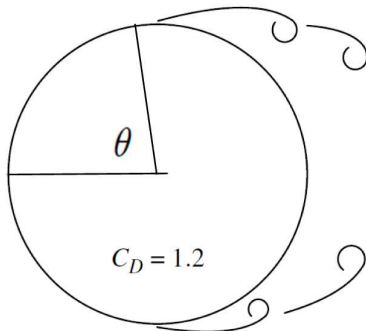
This occur when

$$\left(\frac{\partial u}{\partial y}\right)_0 = 0 \quad (9)$$

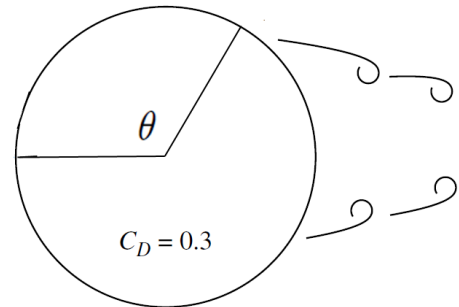
The boundary layer can either be laminar or turbulent. The flow properties are totally different depending on which type of boundary layer it is. The transition from laminar to turbulent boundary layer depends on a variety of properties, but experiments have shown that it occurs at  $Re \geq 10^3$  for a smooth cylinder. However, for a cylinder with rough surface it occurs at a lower Reynolds number.

A laminar boundary layer is very vulnerable to APG on the rear of the cylinder, and separation occurs at a low value of  $\theta$ , see Figure 3a. The resultant wake will be broad and the very low pressure in the separated laminar region cause a large drag coefficient [21].

Turbulent boundary layers are not so sensitive to APG, due to the larger momentum transport, and the separation is delayed to a larger value of  $\theta$ , see Figure 3b. The more narrow wake that are created give a much higher pressure on the rear of the cylinder and the drag coefficient is reduced by 75% compared to a laminar boundary layer. By introducing roughness on the surface such as the dimples on a golf ball, a turbulent boundary layer can be created, resulting in a lower drag force.



(a) Separation in laminar flow



(b) Separation in turbulent flow

Figure 3: Separation angle in laminar and turbulent boundary layer flow [21]

### 2.2.3 Turbulence

In most of the industrial application where CFD is used, the flow is turbulent. Turbulence is very hard to solve and it can be described by following properties [22].

- **Irregularity.** Turbulent flow is irregular and chaotic
- **Diffusivity.** In turbulent flow the diffusivity increases
- **Large Reynolds Numbers.** Turbulent flow occurs at high Reynolds number
- **Three-Dimensional.** Turbulent flow is always three-dimensional and unsteady
- **Dissipation.** Turbulent flow is dissipative
- **Continuum.** The flow can be treated as a continuum

Turbulence models are a time efficient method to model turbulent flows and three different turbulence models, based on the Reynolds Average Navier Stoke (RANS) equations have been investigated in this thesis.

#### Spalart-Allmaras

The Spalart-Allmaras turbulence model was originally developed for the aerospace industry and are, therefore, designed for applications involving wall-bounded flows [23]. The model is a one-equation model that solves a modelled transport equation to determine the kinematic eddy (turbulent) viscosity. The method is much simpler than many other one-equation models and is readily to implement in unstructured CFD solvers [24]. The model has become more and more popular and is today widely used for aerospace applications. For flows past wings where mild separations are expected to occur, the model is accurate as long as the flow not involves complex recirculation and body forces. The model also has been shown to give good result for boundary layers subjected to adverse pressure gradients [24].

#### Realisable $k - \epsilon$

The  $k - \epsilon$  model is a two equation model and one of the most common turbulence models for industrial applications. The transport equations are solved for the turbulent kinetic energy  $k$  and its dissipation rate  $\epsilon$ . The main benefits with the model are the robustness and computational efficiency with reasonable accuracy. The original model has been improved many times and today there exist several different variations of the model [9]. One of these improved version is the realizable  $k - \epsilon$  model that exhibit accurate results for many applications, such as flows involving rotation, boundary layers under strong adverse pressure gradients, separation and recirculation [25]. In these cases, the standard  $k - \epsilon$  model has large drawbacks. The main drawback with the realizable  $k - \epsilon$  model is that it produces non-physical turbulent viscosity.

**SST  $k - \omega$** 

The shear-stress transport (SST)  $k - \omega$  model is an eddy-viscosity model developed by Menter [26]. For applications where viscous flows need to be well resolved and turbulence models are applied throughout the boundary layer has the *SST  $k - \omega$*  model become very popular, such as in the aerospace industry. One of the main novelties of the model is the limitation of the shear stress in APG flows [22].

The model is a combination of a  $k - \omega$  model and a  $k - \epsilon$  model. The standard  $k - \omega$  model has benefits in the near wall region, but perform badly in the free stream and the opposite is true for standard  $k - \epsilon$ . A blending function ensures that the *SST  $k - \omega$*  model behaves appropriately in both near-wall regions where it uses the  $k - \omega$  model, and in the free-stream where it uses the  $k - \epsilon$  model, by switching between the models.

**2.2.4 Introduction to VIV**

VIV is a common phenomenon in several industrial applications dealing with long flexible structures, such as chimneys, cables for bridges and risers. Several research attempts to predict and suppress VIV have been made during the last decades and these attempts will continue. In the offshore industry, VIV researches are of particular interest since the drilling depth increases. VIV is probably the single most important design issue for steel catenary risers, particularly in areas with high currents. The vortex shedding frequency depends on the current velocity and will increase in high currents. This induces high frequency cyclic stresses in the riser, which can result in fatigue damage [27]

Deepwater risers are especially susceptible to VIV because:

1. Currents are typically higher in deepwater areas than in shallower areas.
2. The increased length of the riser lowers its natural frequency and thereby lowering the magnitude of current required to excite VIV.
3. Deepwater platforms are usually floating platforms so that the flexibility of the system is further increased.

The currents in the ocean usually change magnitude and direction and the velocity profile are never uniform. To predict a correct current is probably the most critical part in the model setup. Measurements and experiments must be performed, but these are not sufficient to get accurate current profiles. Multiple modes of the riser can be excited into VIV due to variations in the current profile and diameter changes of the riser. This makes deepwater riser VIV prediction much more complex than that for short risers in shallow water.

If the analysis shows damaging conditions somewhere along the riser, there are some main approaches to improve the design of the riser. A couple of these approaches are connected to the eigenfrequencies of the structure such as changing the mass (e.g. subtracting buoyancy) or increasing the tension. Another common approach is to add VIV suppression devices to reduce the vibration, such as strakes that are used on chimneys. For further reading see [28] and [29].

There are some important parameters governing VIV in risers, these are:

- geometry ( $L/D$ )
- mass ratio ( $m^*$ )
- damping ratio ( $\zeta$ )

- Reynolds number ( $Re$ )
- reduced velocity ( $V_r$ )
- flow characteristics (flow profile, steady/oscillatory flow, turbulence intensity etc.)

The parameters will be explained further in the following section.

### 2.2.5 Vortex shedding

Vortex shedding is an unsteady oscillating flow that takes place at certain conditions when a fluid flows around a body, especially around blunt cylindrical bodies. Vortices are created behind the body and detach periodically from either side of the body and result in a Von Karman vortex street. An asymmetrical flow pattern develops around the body due the periodic shedding and change the pressure distribution behind the body. A low pressure region will follow the vortices and create lift and drag forces on the body. The harmonically varying load that arises from the alternatively shedding induces vibrations with the same frequency as the frequency of the vortex shedding,  $f_s$ . After separation, the regular pattern of vortices moves further downstream and the energy of the vortices is consumed by viscosity and the regular pattern gets dissolved [30].

The vortex shedding process is defined by the Reynolds number and the shedding frequency by the Strouhal number  $St = f_s D / U$  where  $f_s$  is the shedding frequency,  $D$  the diameter of the cylinder and  $U$  the free stream velocity. The Reynolds number can be used to indicate a number of flow regimes. Vortex shedding appears in all these regimes, but with different pattern. Figure 4 show approximately how the vortex pattern depends on the Reynolds number.

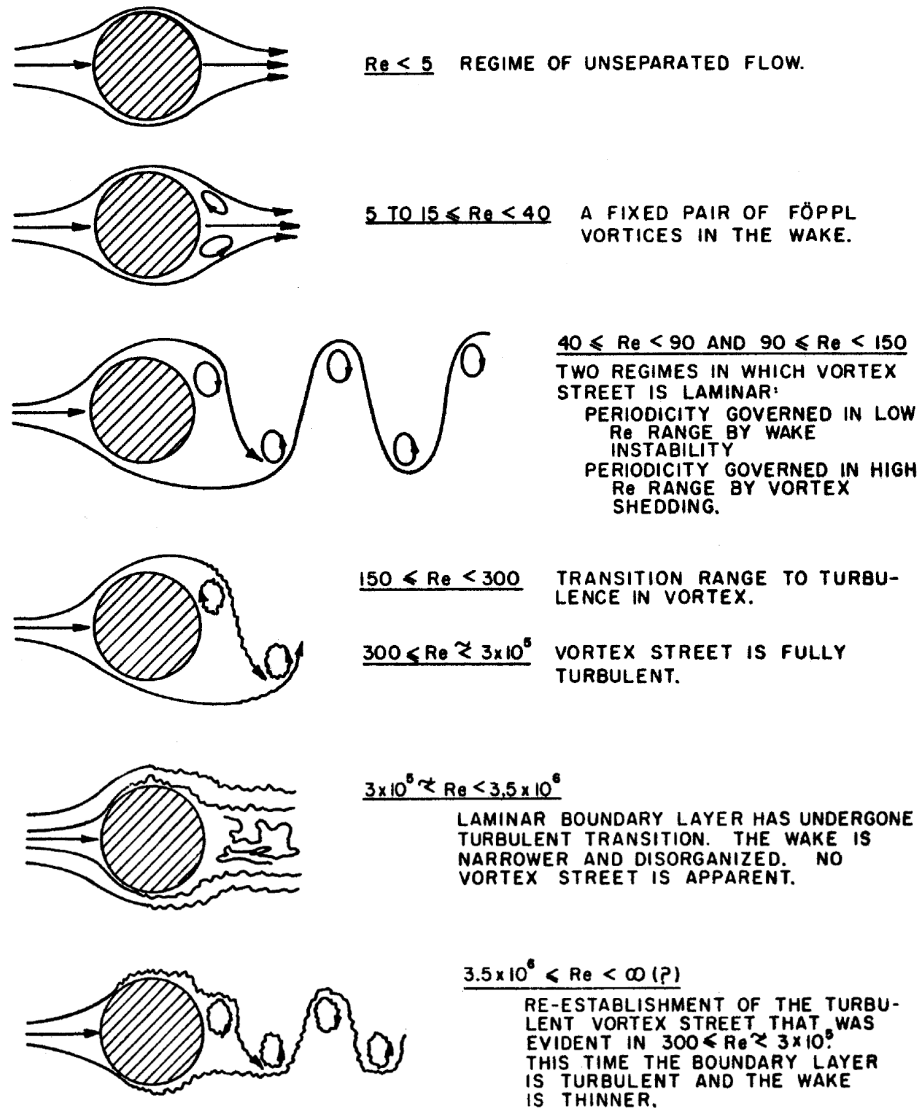


Figure 4: Vortex shedding pattern for different Reynolds number [31]

Both the Reynolds number and Strouhal number depends on the cylinder diameter  $D$  and the flow velocity  $U$ . Experiments have shown that there is a conjunction between the Reynolds number and Strouhal number [31]. These experiments show that the Strouhal number as a function of Reynolds number becomes nearly constant in the sub-critical regime ( $2 \times 10^2 < Re < 2 \times 10^5$ ). The Strouhal number is also strongly dependent on surface roughness and rough surfaced cylinders or vibrating cylinders is relatively insensitive to the Reynolds number. The surface roughness affects where the separation occurs and thereby the regime of Reynolds number. This means that a lower Reynolds number is needed to enter the critical regime if the surface is rough. Reynolds numbers related to risers are in general in the sub-critical regime, which corresponds to  $St = 0.2$ .

### 2.2.6 Lock in

If the vortex shedding frequency is close to one of the natural frequency of a body, it causes resonance and the body starts to vibrate with the same frequency as the shedding frequency, this is called "lock-in" [32] and [33]. Lock-in, sometimes referred as synchronization, is critical



and large damaging vibrations take place when the body becomes "lock-in". It is not obvious when the structure becomes "lock in" and it can occur in a range of frequencies. The span of frequencies is strongly dependent on the mass ratio  $m^*$ , see Equation 10. The lock-in region is larger for smaller mass ratios and becomes critical as the mass ratio goes to unity [34].

$$m^* = \frac{m_s}{m_f} \quad (10)$$

Where  $m_s$  is the mass of the structure and  $m_f$  is the mass of the fluid. In the lock-in region, the vortex shedding frequency is dictated by the eigenfrequency of the structure. As the shedding frequency becomes "lock in" to one of eigenfrequencies of the structure, the relation to the Strouhal number disappears and a new parameter is, therefore, introduced, the reduced velocity ( $V_r$ ), see Equation 11. For velocities higher and lower than the critical lock-in velocity, the shedding frequency follows the Strouhal relationship.

When the structure starts to oscillate, it can move pure In-Line (parallel to the incoming flow, Cross-Flow (perpendicular to the incoming flow) and Cross flow induced In-Line. Pure In-Line motion will occur at the lowest reduced velocities and will be the first response to occur. At higher reduced velocities, the pure In-Line motion is not of particular interest longer, due to low amplitudes, even if its oscillation frequency are twice as the *CF* frequency [35]. Instead of pure In-Line motion a Cross flow induced In-Line motion becomes important for higher reduced velocities. The dominated motion for higher reduced velocities are the *CF* motion followed by the *CF* induced In-Line motion which has an amplitude of 30 – 50% of the *CF* amplitude [36].

### Reduced velocity

When a structure starts to vibrate due to VIV, the reduced velocity becomes useful. The reduced velocity gives information in which velocity ranges VIV can occur. For each eigenfrequency of the structure, the reduced velocity can be determined. Vortex shedding can appear for all reduced velocities, but it is often coupled to the amplitude of the vibration. It has been seen that the vibration amplitude reaches maximum and becomes "lock-in" for different values of the reduced velocity. In [37] it was found that the maximal ratio of the non-dimensional response amplitude  $A/D$ , see Section 2.2.7, was obtained in the range  $5 < V_r < 7$  for sub-critical flow and in [38] that lock-in start at  $V_r > 5$  and reach its maximum at  $V_r = 8$ .

$$V_r = \frac{U}{Df_o} \quad (11)$$

Where  $U$  is the free-stream velocity,  $D$  the cylinder diameter and  $f_o$  the natural frequencies for the structure.

#### 2.2.7 A/D

The non-dimensional response amplitude  $A/D$  is one of the most interesting results for VIV analysis on risers. The response amplitude  $A$  can be measured in the flow direction, but is in general measured in the cross-flow direction, as this amplitude is much larger. The cross-flow response is of nature self limiting, meaning that the excitation breaks down for a limited amplitude. The reason for the self limited response is that large vibrations will destroy the harmonic Vortex shedding process and no additional energy from the fluid will be received.

For rigid cylinders with very low damping, the peak amplitude  $A$  is dependent on Reynolds number over a narrow range of reduced velocities. A variety of equations describing the relationship between the ratio  $A/D$  and the Reynolds number has been derived. Equation 12 is derived by [34] and show a linear response versus an logarithmic expression based on the Reynolds number.

$$\frac{A}{D} = \frac{A_{max} - A_{min}}{2D} \approx \log(0.41Re^{0.36}) \quad (12)$$

Where  $A_{max}$  is the maximum response amplitude and  $A_{min}$  the minimum response amplitude.

### 2.2.8 Added mass

Added mass,  $m_a$ , plays a significant role on structures submerged in water, particularly for low mass ratios. For non vibrating cylinder, the added mass is clearly defined and equal to the mass of the displaced liquid, see Equation 13. To define the added mass for structures exposed to VIV is much more complex and its behavior is not easy to define. The added mass coefficient,  $C_a$  is a function of the local flow condition, the oscillation frequency and the cross section geometry [29] and it is equal to unity for non vibrating cylinders. For structures in motion, the acceleration gives rise to changes of the added mass coefficient and it can both be negative and positive.

$$m_a = \rho_f C_a \pi r^2 \quad (13)$$

### 2.2.9 Drag- and lift coefficient

The forces acting on the cylinder due to the flow can be divided into drag and lift forces. In steady flow, the forces depend on the fluid density  $\rho_f$ , the fluid velocity  $U$  and the reference area  $A_\perp$ . The drag force is also depending on the drag coefficient  $C_D$  and the lift force on the lift coefficient  $C_L$ . The periodicity of vortex shedding leads to fluctuations of the force coefficients and these are denoted  $C'_D$  and  $C'_L$  respectively. By taking the root mean square (r.m.s) of the fluctuations it is easy to compare the different flows.

In an ideal flow, the drag force is zero, but becomes non-zero in a real flow, due to pressure and shear forces. Drag forces on a fixed cylinder can fairly easily be determined by Equation 14, where the drag coefficient  $C_D$  is measured in experiments for several of shapes and Reynolds numbers.

$$F_D = C_D \frac{1}{2} \rho_f U^2 A_\perp \quad (14)$$

With the drag force  $F_D$ , the fluid density  $\rho_f$ , the free stream velocity  $U$  and the projected area  $A_\perp$ . The drag coefficient on a smooth fixed cylinder in a laminar boundary layer flow are fairly constant in the range  $10^4 < Re < 5 \times 10^5$ . For the ratio  $L/D = 20$  is  $C_D = 0.91$  and for the ratio  $L/D = \infty$  is  $C_D = 1.2$  [21].

When coming to VIV, these values are not longer valid and new expressions have been derived in [39]. Several researches have tried to find an analytical expression on the drag amplification factor in VIV flow. The drag amplification factor is multiplied with the local drag coefficient for a stationary cylinder, see Equation 15 and can be as large as 2.31 for a ratio of  $A/D = 1$

$$C_D(z) = C_{Do} * C_{D,amp} \quad (15)$$

$$C_{D,amp} = 1 + 1.043 \left( \frac{2y_{rms}}{D} \right)^{0.65} \quad (16)$$

The lift force, Equation 17 is one of the most important coefficients that affect VIV.

$$F_L = C_L \frac{1}{2} \rho U^2 A_\perp \quad (17)$$

The r.m.s lift coefficient is defined as:

$$C'_L = \frac{2L'}{\rho U^2 D \ell_c} \quad (18)$$

where  $L'$  is the r.m.s of lift fluctuations acting on a spanwise segment of length  $\ell_c$ . The total lift fluctuations are given by letting  $\ell_c = \ell$ , where  $\ell$  is the total length of the cylinder.

### 2.3 Structural theory

The equation of motion for a pipe undergoing VIV can be written as [40]:

$$\mathbf{M}(\mathbf{u})\ddot{\mathbf{u}} + \mathbf{C}(\mathbf{u})\dot{\mathbf{u}} + \mathbf{K}(\mathbf{u})\mathbf{u} = \mathbf{f}_{\text{top}} + \mathbf{f}_{\text{drag}} + \mathbf{f}_{\text{TLP}} \quad (19)$$

Where  $\mathbf{M}$ ,  $\mathbf{K}$  and  $\mathbf{C}$  are the mass, stiffness and damping matrix;  $u$ ,  $\dot{u}$  and  $\ddot{u}$  the displacement, the velocity and the acceleration. The forces  $\mathbf{f}_{\text{top}}$  and  $\mathbf{f}_{\text{drag}}$  are the top tension, drag force from current and riser motion. The force  $\mathbf{f}_{\text{p}}$  is forces due motion of the platform.

#### 2.3.1 Morison equation

In more than 50 years has the so-called *Morison equation* been used to calculate hydrodynamic loads on small-diameter submerged objects, such as risers. The equation is widely used, even though the equation has been considered to be controversial. The equation combines structural motions with external fluid motion to calculate the resulting hydrodynamic forces.

$$f(x) = \frac{1}{2}\rho C_D \phi(u - v)|u - v| + \rho A_e \dot{u} + (C_M - 1)\rho A_e(\dot{u} - \dot{v}) \quad (20)$$

Where  $(C_M - 1)\rho A_e$  is termed added mass and  $C_M = (C_a + 1)$  the inertia coefficient. A value of the inertia coefficient is typically close to two, which correspond to a value of the added mass coefficient  $C_a = 1$ .

#### 2.3.2 Mode-Superposition of an undamped structure

The equation of motion of a linear Multi Degree Of Freedom, MDOF, system with  $N$  unknowns are

$$\mathbf{M}\ddot{\mathbf{u}} + \mathbf{C}\dot{\mathbf{u}} + \mathbf{K}\mathbf{u} = \mathbf{f} \quad (21)$$

In general, the coefficient matrices ( $\mathbf{M}$ ,  $\mathbf{C}$  and  $\mathbf{K}$ ) are large and have nonzero coupling terms, then the required number of equations is large. The mode-superposition method is an effective approach to reduce the number of unknowns in a dynamic response analysis. The basic idea is to uncouple a set of equations by solving the eigenvalue problem. The uncoupled equations can be solved independently, which reduces the complexity of the problem significantly. An approximate solution can be found by solving the system for only a small amount of the total number of modes. The general procedure in the mode-superposition approach using all numbers of modes are described below [41]

The first step is to determine the natural eigenfrequencies and natural modes of the undamped system. Solving equation 21 with the initial conditions

$$\mathbf{u}(0) = \mathbf{u}_0, \quad \dot{\mathbf{u}}(0) = \dot{\mathbf{u}}_0 \quad (22)$$

The following eigenvalue problem will be obtained.

$$[\mathbf{K} - \omega_r^2 \mathbf{M}]\phi_r = 0 \quad (23)$$

Where  $r = 1, 2, \dots, N$  and the modes  $\phi_r$  are assumed to be normalized. The modal masses  $M_r$  and the modal stiffnesses  $K_r$  are given by

$$M_r = \phi_r^T \mathbf{M} \phi_r, \quad K_r = \phi_r^T \mathbf{K} \phi_r \quad (24)$$

For repeated frequencies it is assumed that the associated modes can be orthogonalized so that the orthogonality equations

$$\phi_r^T \mathbf{M} \phi_s = \phi_r^T \mathbf{K} \phi_s = 0 \quad (25)$$

are satisfied for all  $r \neq s$ . All modes can then be collected into a modal matrix

$$\Phi = [\phi_1 \ \phi_2 \ \dots \ \phi_N] \quad (26)$$

Then Equation 24 and 25 can be combined and written as

$$\mathbf{M} = \Phi^T \mathbf{M} \Phi = \text{diag}(M_r) \quad \mathbf{K} = \Phi^T \mathbf{K} \Phi = \text{diag}(K_r) = \text{diag}(\omega_r^2 M_r) \quad (27)$$

The most important step to convert the coupled equations to uncoupled equations is to introduce a coordinate transformation. The coordinate transformation are given in Equation 28. These new coordinates are defined as  $\eta_r(t)$  and called principal coordinates or modal coordinates.

$$\mathbf{u}(t) = \Phi \boldsymbol{\eta}(t) = \sum_{r=1}^N \phi_r \eta_r(t) \quad (28)$$

By inserting this into Equation 21 and multiplying the resulting equation by  $\Phi^T$ , then the final equation of motion expressed in modal coordinates is

$$\mathbf{M} \ddot{\boldsymbol{\eta}} + \mathbf{C} \dot{\boldsymbol{\eta}} + \mathbf{K} \boldsymbol{\eta} = \mathbf{f}(t) \quad (29)$$

### 3 Benchmark

Two different methods to solve FSI problems have been studied in this thesis. The first method applies mode-superposition and is performed in AcuSolve. The second method is a fully partitioned system applying an iterative coupling between Abaqus and STAR-CCM+. To investigate if the evaluated methods are suitable for solving FSI-problems concerning flexible bodies, a benchmark problem has been solved. The benchmark problem was originally defined by Turek & Hron [42] and solved in a monolithic approach. This benchmark problem is widely used and popular for investigation of crucial problems with low density ratios between the structure and the fluid.

#### 3.1 Software

The structural solver used in this benchmark is Abaqus and the fluid is solved by AcuSolve and STAR-CCM+. The later analysis in Section 5 and in Section 6 are solved with a coupling between Abaqus and STAR-CCM+.

##### 3.1.1 Abaqus 6.12

All structural computations have been performed in Abaqus. Abaqus is a general purpose finite element software and one of the most popular in the industry [43]. The fluid domains for both the benchmark problem and the short riser, see Section 5.1.1 have been defined in Abaqus and exported to both AcuSolve and STAR-CCM+. The frequency analysis used to perform the mode-superposition in AcuSolve must be done in Abaqus 6.11 since AcuSolve 1.8b is not compatible with the odb-file from Abaqus 6.12.

##### 3.1.2 AcuSolve 1.8b

AcuSolve is a FEM based CFD solver developed by AcuSim. AcuSolve is based on the Galerkin/Least-Squares formulation. AcuSolve uses a fully coupled pressure/velocity iterative solver plus a generalized alpha method as a semi-discrete time stepping algorithm. AcuSolve is a general purpose incompressible flow solver that use unstructured meshes and apply ALE to move the mesh, see [44] and [45]. AcuSolve is a popular code to solve VIV of risers and providing two methods to solve FSI problems called Practical FSI (P-FSI) and Direct Coupled FSI (DC-FSI).

##### 3.1.3 STAR-CCM+ 7.04.006

STAR stands for *Simulation of Turbulent flow in Arbitrary Regions* and it is developed by CD-adapco. STAR-CCM+ is based on an object-oriented programming technology and specifically designed to handle large models efficiently. The software uses a finite volume approach and it is possible to solve problems involving flow of fluids, deformation and stress analysis of solids and heat transfer [46]. STAR-CCM+ apply morphing to move the mesh.

#### 3.2 Method benchmark

Three different parameters have been evaluated for the model in STAR-CCM+, the free end displacement in y-direction, the drag force and the lift force. The evaluation also includes a study of how the mesh size and the time step affect the results. Only one mesh with one time step is studied in AcuSolve. A complete comparison between STAR-CCM+ and AcuSolve is not possible. STAR-CCM+ and AcuSolve are based on two totally different solution techniques and the same settings of the solvers are not available and different meshes with different element types are used. A control point for the free end displacement is placed at the coordinate (0.6m, 0.2m, 0.0025m).

### 3.2.1 Geometry

The geometry was originally constructed and used for a CFD benchmark, where flow around a fixed circular cylinder was studied. Turek & Hron added an elastic flag behind the cylinder to create this FSI benchmark. The height of the domain is  $H_D = 0.41m$  and the length  $L_D = 2.5m$ . The circle has a radius of  $r = 0.05m$  and the dimensions of the flag are  $L_F = 0.35m$ ,  $H_F = 0.02m$ . The circle and the flag are not located in the center of the domain. The non-symmetric location of the circle makes it possible to get the same oscillation conditions for all test cases. The center of the circle are located at  $C = (0.2m, 0.2m)$  The domain has a thickness of  $t_D = 0.005m$

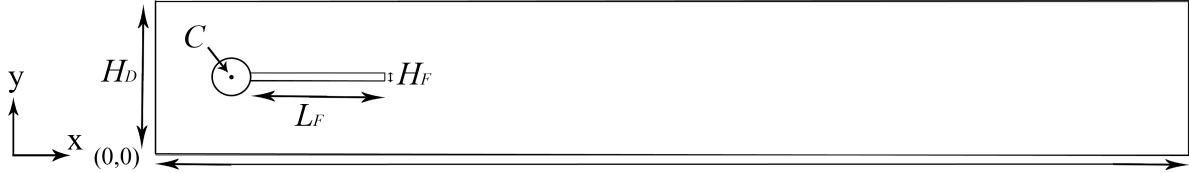


Figure 5: Domain for Benchmark problem

### 3.2.2 Structural mesh

Two different structural meshes have been created with purpose to investigate element types and grid size. The first mesh, *Mesh 1s*, see Figure 6 is meshed with 560 linear hexahedral elements of type C3D8I (The *I* stands for Incompatible modes). There are four elements in y-direction, two elements in z-direction and 70 elements in x-direction. In the second mesh, *Mesh 2s*, see Figure 7 the flag is meshed with 2240 linear hexahedral elements of type C3D8R (The *R* stands for Reduced integration). There are eight elements in y-direction, two elements in z-direction and 140 elements in x-direction. For further reading about structural elements, see [43].

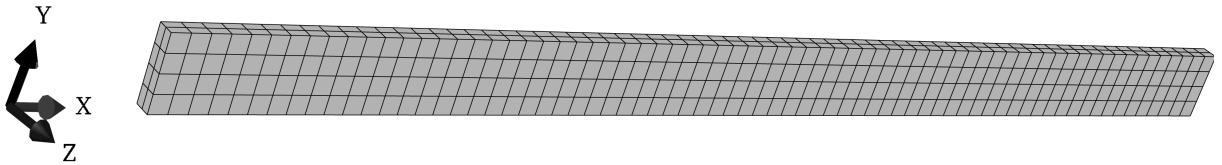


Figure 6: Flag with coarse mesh, *Mesh 1s*

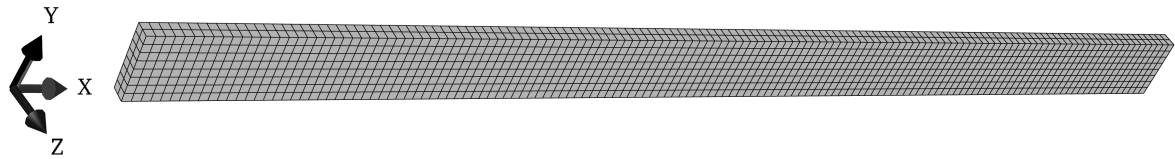


Figure 7: Flag with fine mesh, *Mesh 2s*

### 3.2.3 Material properties

The material for the flag is a combination of two rubber-like materials, polybutadiene and polypropylene. These materials have very low stiffness, which makes it possible to obtain large deformations of the flag, even if the forces acting on it, are relative small. Young modulus for the resulting material is  $E_s = 5.6MPa$  and the Poisson ratio  $\nu_s = 0.4$ . The density of the flag,  $\rho_s$  is set to  $10^3 \frac{Kg}{m^3}$  which give a mass ratio  $m^* = 1$ . These properties make it possible to investigate the stability in the coupling with low mass ratios. An additional damping  $\beta = 0.0002$  has been

introduced in the material to increase the stability.

The fluid properties are similar to glycerin that is an viscous liquid with relative high density. For simplicity, small adjustments for the dynamic viscosity  $\nu_f$  and the density  $\rho_f$  has been made which results with  $\nu_f = 0.001 \frac{m^2}{s}$  and  $\rho_f = 10^3 \frac{Kg}{m^3}$ .

### 3.2.4 STAR-CCM+

#### Fluid mesh

Three different mesh configurations have been studied, and all configurations apply a refinement block with the dimension  $0.23m \times 1.02m \times 0.005m$ . The first mesh, *Mesh 1*, is a coarse mesh with 27549 hexahedral cells and two boundary layer cells around the cylinder with equal thickness of  $0.00125m$ . The cell sizes in the refinement block are  $0.005m \times 0.005m \times 0.0025m$ . The second mesh, *Mesh 2*, see Figure 8 has medium refinements in the domain and the block. *Mesh 2* contains of 119500 hexahedral cells and two boundary layer cells around the cylinder with equal thickness of  $0.00125m$ . The cell sizes in the refinement block are  $0.0025m \times 0.0025m \times 0.0025m$ . The third mesh, *Mesh 3* contains of 552420 hexahedral cells and five boundary layer cells around the cylinder. The thickness of first cell is  $0.0004m$  and the total thickness of the prism layer is  $0.003m$ . The cell sizes in the refinement block are  $0.0015m \times 0.0015m \times 0.0015m$ .

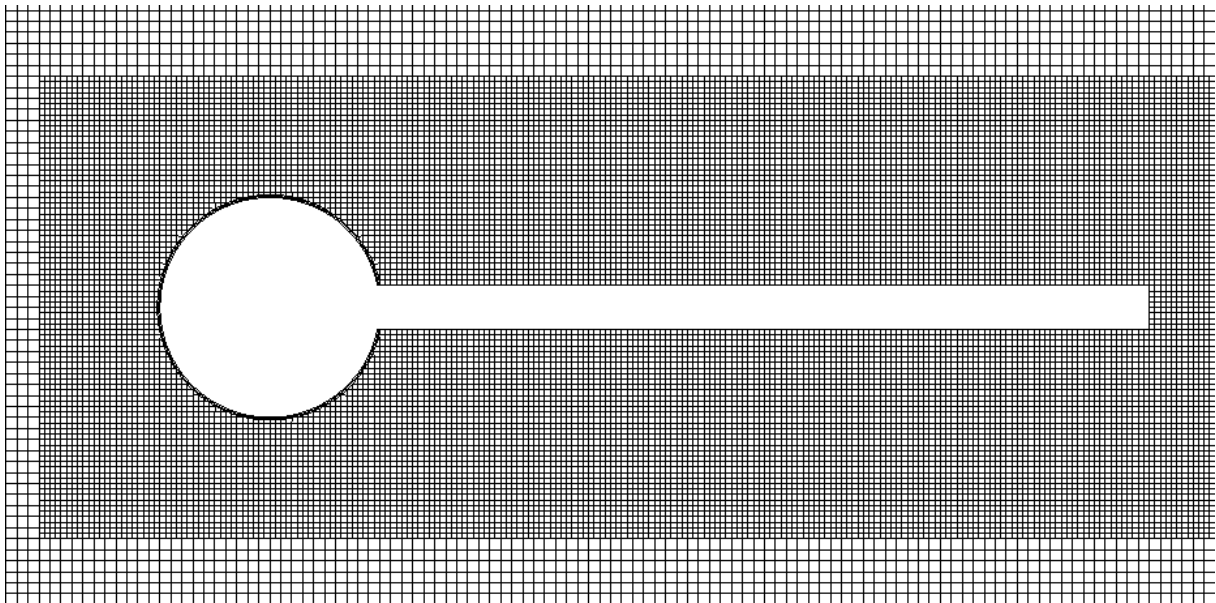


Figure 8: A zoom on the flag for *Mesh 2*

#### Set-up

An overview of the basic settings in the STAR-CCM+ model is shown in the following table.

Table 1: Simulation settings for benchmark in STAR-CCM+

Settings	Choice
Temporal discretization	2 <sup>nd</sup> order
Convection scheme	2 <sup>nd</sup> order upwind
Viscous regime	Laminar
Flow	Segregated
Time model	Implicit unsteady
Solver algorithm	SIMPLE
Default Time Step	
<i>Mesh1</i>	0.004 s
<i>Mesh2</i>	0.001 s
<i>Mesh3</i>	0.001 s

One of the main assumptions in the model is that the liquid is compressible, which makes the density dependent on the working pressure. By changing the speed of sound, influence of the pressure is regulated. For more details on compressible liquids see [9]. Three different time steps are evaluated for *Mesh1*, these are, 0.001s, 0.004s and 0.01s. For the case with a time step of 0.01s, both 20 and 30 inner iterations are evaluated.

Within each time step, a number of inner iterations are performed. The number of inner iterations are used to ensure that both the flow and the imported displacement have converged. 20 inner iterations are used for *Mesh 1* and 30 inner iterations are used for *Mesh 2* and *Mesh 3*. Increasing the number of inner iteration to 30 makes it possible to get convergence with a time step of  $\Delta t = 0.001$

The *Field Exchange Controls* is automatically visible when a Co-simulation with iterative coupling are defined. The *Inner Iterations Per exchange* controls the number of inner iterations STAR-CCM+ performs for each field data exchange within one coupling time-step. How many exchanges of data between STAR-CCM+ and Abaqus that are required within each time step depends on how critical the problem is. Since this problem requires a strong coupling only one inner iteration will be performed between each Co-Simulation coupling.

The flag is a very flexible structure and can easily be unstable if large forces are applied on the surface at one moment. To get a smooth start of the coupling, the velocity and the pressure are recommended to gradually increase. Only the pressure is ramped in this study and the ramp-up time is 0.2s.

The under relaxation for velocity and pressure is another parameter that must be taken into account. In the first iteration of a time step, the updated displacements that Abaqus export are fairly accurate (amount the interface moves if the pressure had been constant). However, using the default velocity under-relaxation of 0.7 forces an error into that first estimate Abaqus export, tending to decelerate/accelerate the fluid with respect to the true solution, causing the pressure to jump up/down accordingly in that first iteration. Increasing the under-relaxation must be done with caution and monitoring the pressure at interesting point and the convective Courant number in the entire domain is important. If the convective Courant number is much greater than one anywhere in the fluid mesh may cause the solution to diverge [47].



### 3.2.5 AcuSolve

#### Fluid mesh

A well constructed mesh has shown to be very important to get a working model in AcuSolve. The mesh must be good enough so that vortex shedding start and not distort to much when the flag start to move.

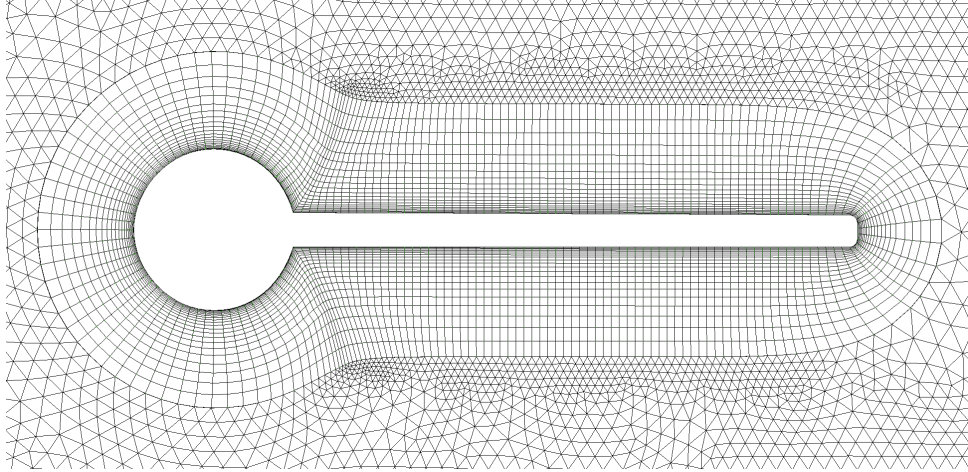


Figure 9: A zoom on the flag for *Mesh – AcuSolve*

#### Set-up

To find settings that makes it possible to solve the benchmark problems has not been easy and suitable settings has not been found. The following settings has shown to give a fairly stable solution.

Table 2: Simulation settings for benchmark in AcuSolve

Settings	Choice
Temporal discretization	2 <sup>nd</sup> order (Generalized Alpha)
Space discretization	Galerkin/Least-Squares FEM
Viscous regime	Laminar
Flow equation	Navier Stoke
Time model	Implicit
Time Step	0.00001-0.001 s

Two of the most important parameters to obtain a steady solution in AcuSolve are the number of Krylov vectors and the number of stagger iterations. For this benchmark, 40 Krylov vectors and 40 maximum stagger iterations are defined.

It has been shown that a very small time step together with several Krylov vectors and stagger iterations is required to avoid mesh distortion. The computational time with these settings will be very long and automatic time incrementing is applied. The automatic time incrementing make it possible to use a small time step when in critical situations and a large time step otherwise.

### 3.2.6 Boundary condition

The problem is solved in 3D, but it can be described as a structure submerged in a 2D channel flow, where the inlet is located and the left boundary and the outlet at the right boundary. The upper and lower boundaries are walls and the surfaces with normal out of plane are a symmetry surface. The displacement at the left end of the flag is fixed and the normal surface is fixed in z-direction and unable to rotate around the x- and y-axis. The following settings are used for all simulations.

Table 3: Boundary conditions for benchmark

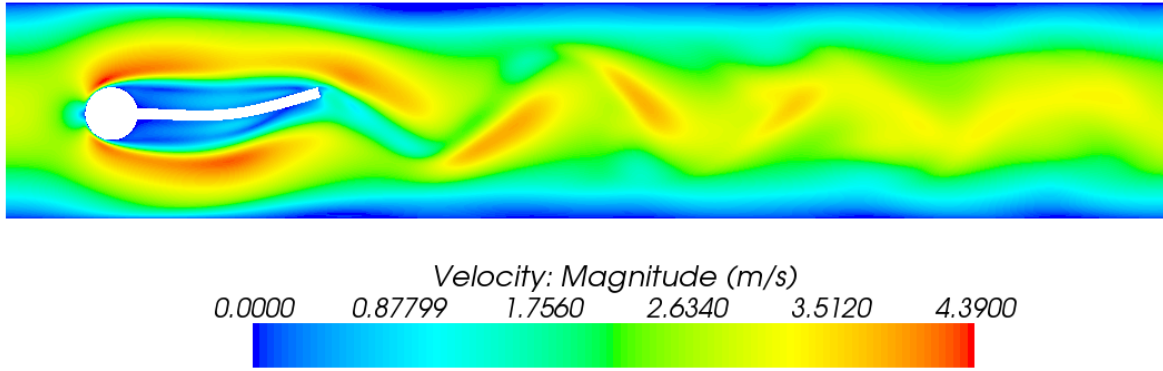
Settings	Choice
<i>Boundary conditions fluid:</i>	
Inlet	Velocity inlet
Outlet	Pressure outlet
Upper wall	No-slip wall
Lower wall	No-slip wall
Symmetry	Symmetry plane
Cylinder	No-slip wall
Flag	Co-Simulation/Flexible body
<i>Boundary conditions structure:</i>	
Left end	Pinned
Symmetry	Z-symmetry( $\delta z = UR_x = UR_y = 0$ )

The inlet velocity has a parabolic profile with a mean velocity  $\bar{U} = 2m/s$ , defined as

$$v_f(0, y) = 35.69\bar{U}y(0.41 - y) \quad (30)$$

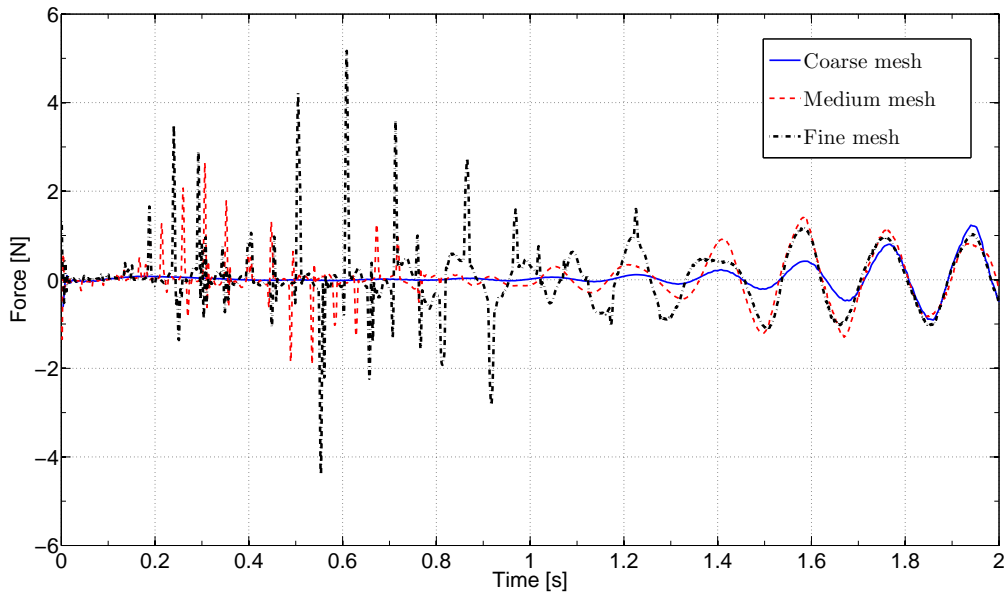
## 3.3 Results benchmark

The presented results are the y-displacement of the flags free end, drag forces and lift forces and the free end displacement is compared with values from *Turek&Hrons* analysis. The free end displacement is measured in y-direction and the drag- and lift force are computed by adding the forces acting on both the cylinder and the flag. The coupling has shown to be more unstable as long as the flow develops in the channel. The first part of this chapter has focus on the time where the flow develops and the second part on a fully developed flow. The fine mesh, *Mesh3* is only used for analysis in the developing flow. No results from the AcuSolve analysis is presented since no working model is found. Figure 10 illustrates the velocity field and the deformation of the flag in a fully developed flow.

Figure 10: A fully developed flow with *Mesh 2*

### 3.3.1 Developing flow

The developing part of the flow has shown to be unstable, due to numerical difficulties. The instabilities is clearly depicted in Figure 11. Vortex shedding does not start directly and Figure 12 shows how the y-displacement is affected by the three meshes. The oscillations for *Mesh1* begins later, but increase in the same manner as for *Mesh2*.

Figure 11: Lift force for *Mesh1*, *Mesh2* and *Mesh3*

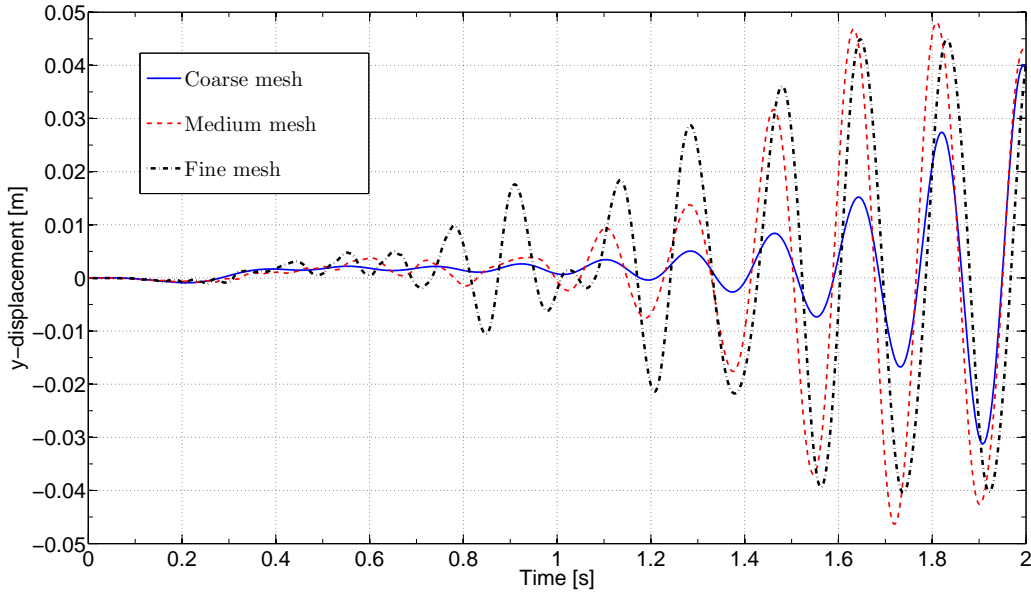


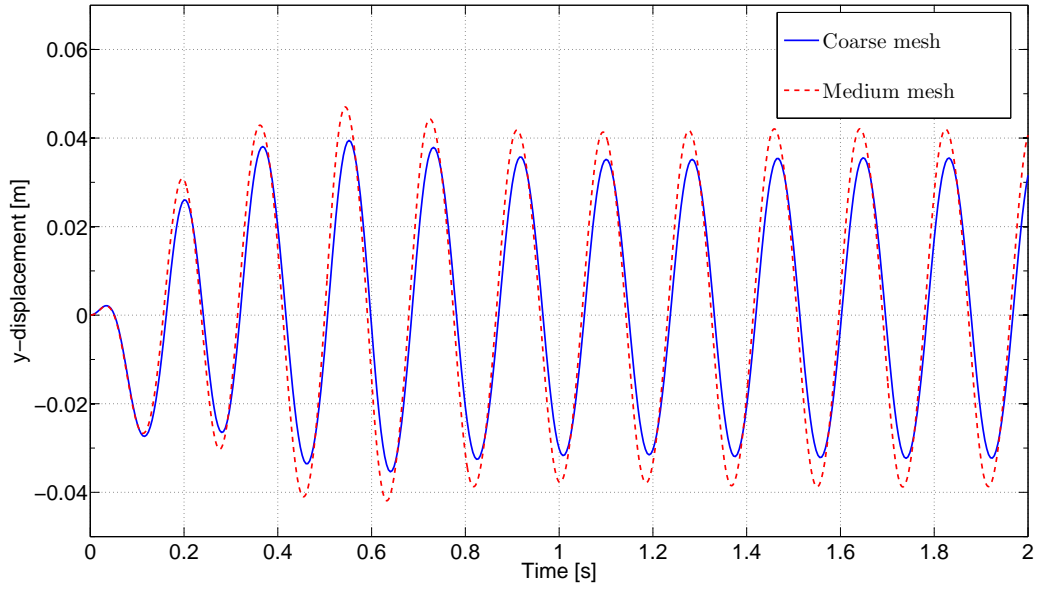
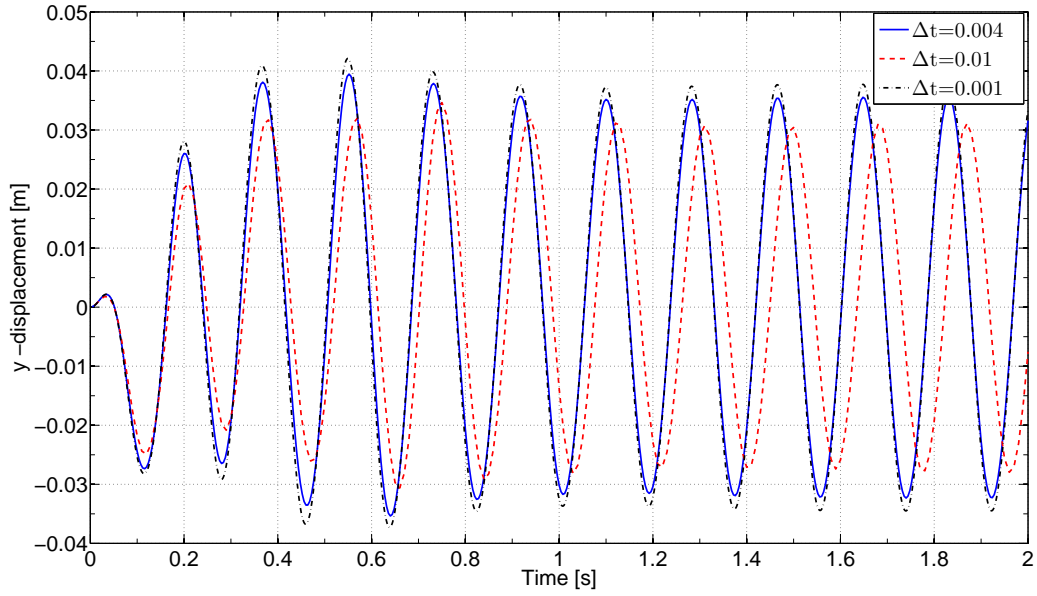
Figure 12: Free end y-displacement for *Mesh1*, *Mesh2* and *Mesh3*

### 3.3.2 Fully developed flow

Simulating the initial part, where the flow develops with a fixed flag avoids problems related to the instabilities in the initial part. The flag holds fixed until the flow is developed and vortex shedding has started. After approximately 1.8s, the restriction with a fixed flag is removed and it is free to move. All simulations in this section start from the moment where the flag start to move and  $t = 0$  in these simulations correspond to  $t \approx 1.8s$  in the simulations where the flow developed. The coupling procedure is time-consuming and starting to simulate with a fully developed flow save much time.

#### Free end displacement

*Turek&Hron* found that the free end displacement  $uy$  converges at  $uy_o = 1.48 \pm 34.38mm$  which gives a maximum displacement of  $uy_o = 35.85mm$ . Figure 13 shows that the maximum displacement for *Mesh1* is  $uy_1 = 35.37mm$  and for *Mesh2*  $uy_2 = 42.06mm$ . The shedding frequency is not affected when the mesh is refined and not either when decreasing the time step. An increase of the time step results on the other hand in a lower shedding frequency as one can see in Figure 14. The y-displacement for the free end is also affected by the time step. A smaller time step corresponds to a larger magnitude of the displacement a larger time step to a smaller magnitude of the free end y-displacement.

Figure 13: Free end y-displacement for *Mesh1* and *Mesh2*Figure 14: Free end y-displacement with different time step for *Mesh1*

### Drag force

The drag forces behaves similar as the free end displacement, but the mesh dependency is more pronounced for the drag force, see Figure 15. Much larger drag forces are obtained with *Mesh 2* than with *Mesh 1* and larger drag forces are also related to a small time step.

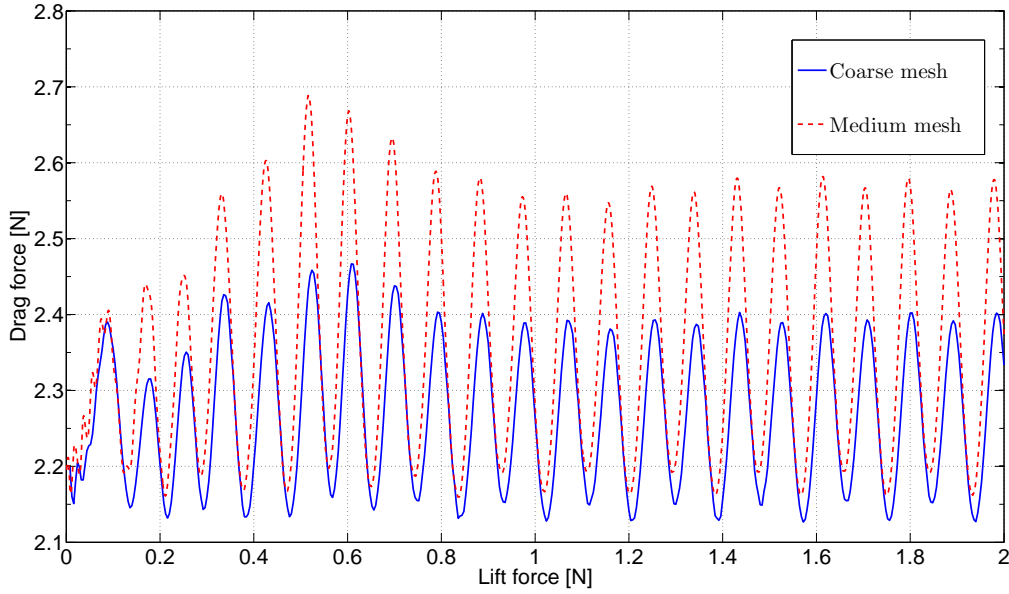


Figure 15: Drag force for *Mesh1* and *Mesh2*

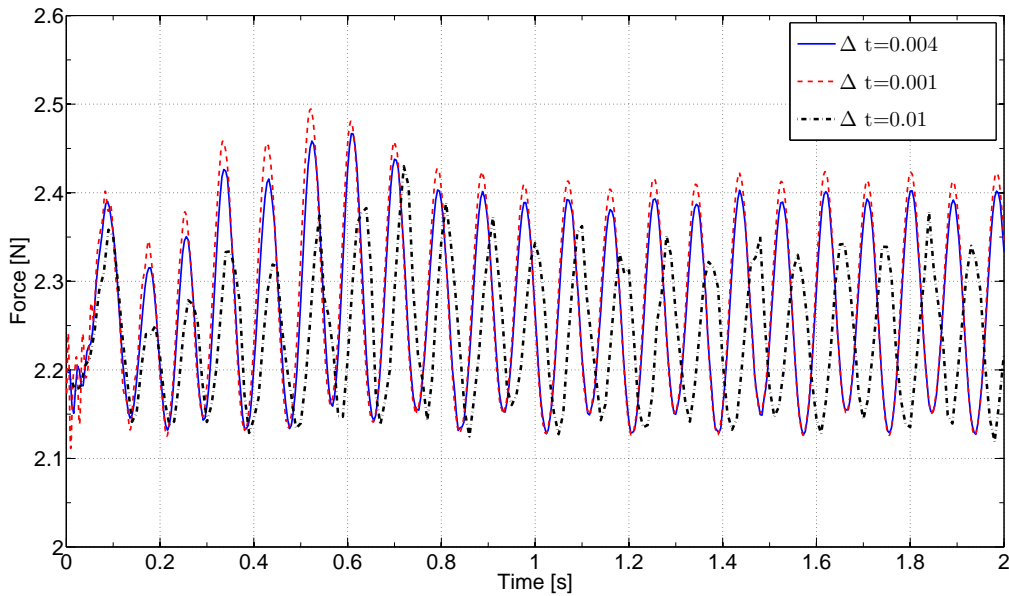


Figure 16: Drag force for *Mesh1* with different time steps

### Lift force

The lift force is not affected by the time step in same extend as the drag force.

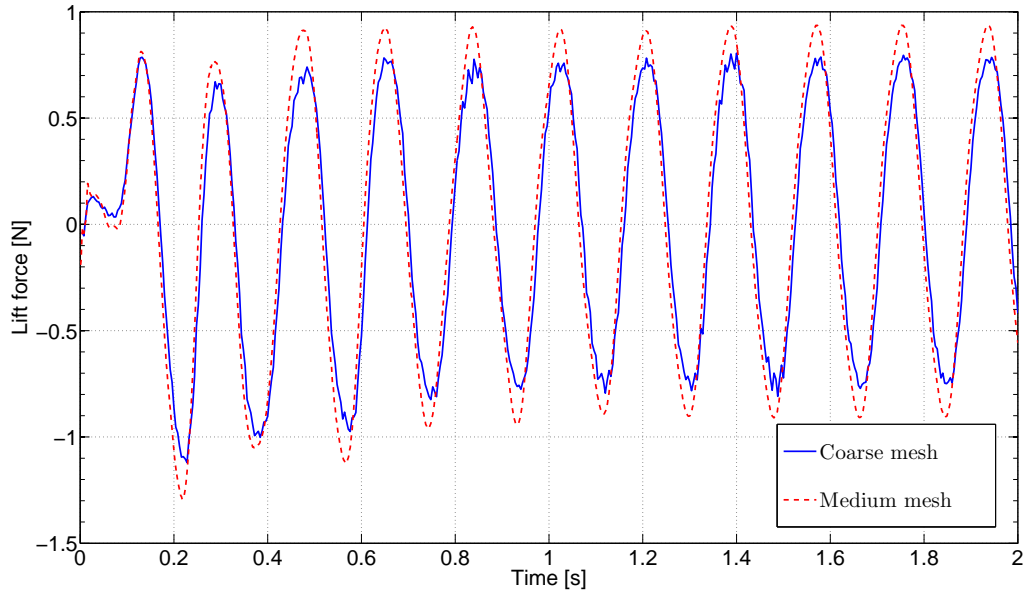


Figure 17: Lift force for *Mesh1* and *Mesh2*

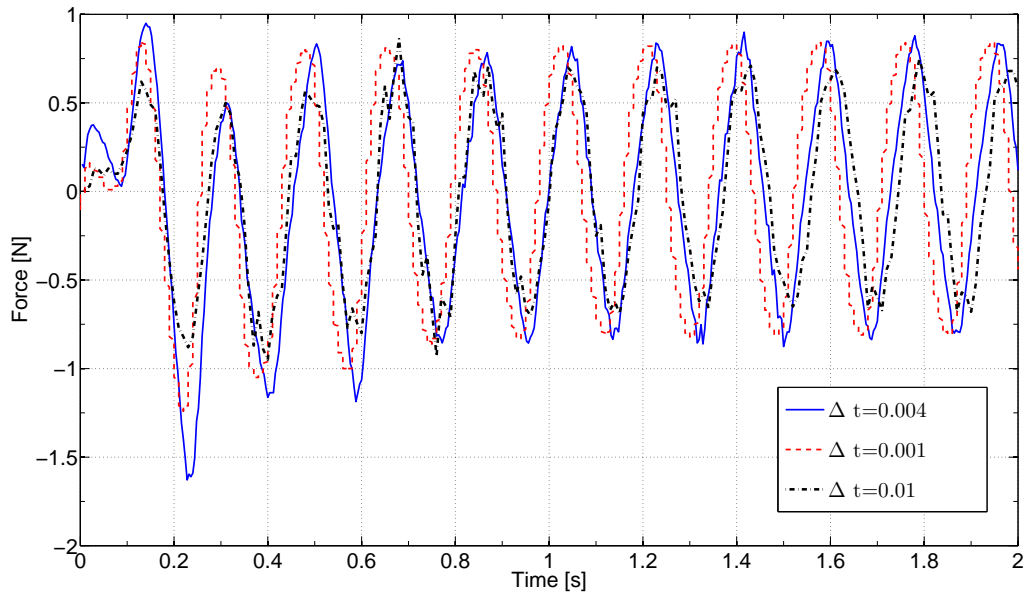


Figure 18: Lift force for *Mesh1* with different time steps

Decreasing the time step has shown to over predict the displacements and the forces. However, with a small time step a more steady solution is obtained. The lift force for each iteration with  $\Delta t = 0.004$  is much more unsteady than with  $\Delta t = 0.001$ .

### 3.4 Discussion benchmark

This benchmark problem is rather complicated and it is difficult to get stability in the coupling, even if an iterative coupling approach is applied in both AcuSolve and between Abaqus and STAR-CCM+. Increasing the number of stagger iterations and Krylov vectors in AcuSolve and coupling steps between Abaqus and STAR-CCM+ within each time step, are important parameters, but not the only ones.

The number of coupling iterations required to get convergence for the coupling procedure depends on how much the flag deforms or moves in one time step. The most favorable is that the flow and the coupling iteration converge at the same inner iteration. Each coupling iteration is quite time-consuming and in general, the coupling procedure converges faster than the flow. Hence, to couple every second or third flow iteration can be desirable. For this benchmark the motion of the flag is large and it is necessary to couple at each flow iteration.

A comparison with the results in *Turek&Hron* study shows an over prediction of the displacement and the forces, as the time step decreases and the mesh is refined, opposite to that expected. However, a small time step provides a smoother and more steady solution. Increasing the time step to  $\Delta t = 0.01$  is not to recommend, even if the number of inner iterations increases. The forces are lower as well as the shedding frequency and this probably related to a too large convective Courant number. However, deviations from *Turek&Hron* analysis has been shown also in other comparisons analysis [48].

One important parameter for analysis of flexible bodies is the ability to follow the structural motion. The mesh motion in AcuSolve is based on ALE, see Section 2.1.3. The main problem with AcuSolve is distortion of the mesh when the acceleration of the structure becomes large. This occurs when the free end displacements is large and the oscillation frequency high. A proper definition of the nodes that not deforms and only follow the motion of the structure is decisive. The fluid mesh in AcuSolve must be created with high quality to avoid mesh distortion of the fluid mesh. The mesh and the time step has shown to be the most critical parameters to obtain stability in analysis performed in AcuSolve. In the analysis performed in STAR-CCM+, the fluid mesh has very little to do with the stability. STAR-CCM+ apply a morphing technique to move the fluid mesh, see Section 2.1.3. The morphing technique has been shown to be capable to handle large motions of the structure.

It was much easier to create a working model in STAR-CCM+ than in AcuSolve. By making the fluid slightly compressible, the most unrealistic deformations of the structure can be avoided. When using the correct material properties it has been found that a slightly compressible fluid is the only way to get convergence for the STAR-CCM+ model. Other parameters, such as mesh quality, inner iterations and time steps does not affect the stability significant. The forces and displacements are over predicted compared to *Turek&Hron* analysis and it can be related to the compressible fluid. The effect of making the fluid compressible should be studied further.

Refining the structural mesh does not affect the accuracy in the result noticeable, but the computational time increase significantly. A further study of structural elements and how the computational time can be reduced is recommended.



## 4 Riser analysis

To determine if the riser is expected to undergo VIV or not for a given condition, several difficult aspects are involved. The guiding parameter for VIV is the reduced velocity, see Section 2.2.6. The range of reduced velocities that VIV are expected to occur in is not definite, and depending on prevailing conditions this range will change. However, the reduced velocity depends on both velocity of the current and the eigenfrequencies of the structure. These parameters are not easy to determine exactly and therefore, the reduced velocities only are approximations. The purpose of this analysis is firstly, to determine if Abaqus and SHEAR7 give comparable results in terms of the eigenfrequencies of the riser. Secondly, to investigate which velocity profiles that may result in VIV and how many and which modes it applies to. The difference between the eigenfrequencies is small, and in the reality it is expected that more than one mode will be excited for long and flexible risers. Only small deviations of eigenfrequencies can result in large errors in the VIV analysis.

### 4.1 Method preparation work

#### 4.1.1 Geometry

A principal sketch of the modelled riser system is shown in Figure 19. The system contains several different parts and consists mainly of pipe elements, except from the sections at the seabed which are rigid and not of interest in VIV analysis. The main part of the riser system is the Dual Bore and the total length of the Dual Bores is 90% of the total length of the riser below the water surface. The Dual Bore is very long and slender and therefore critical in a VIV perspective.

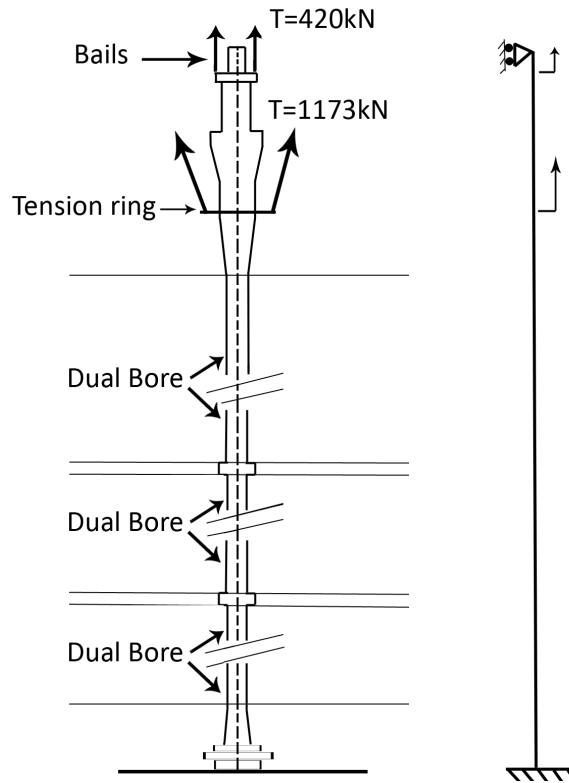


Figure 19: Principal sketch of riser system and associated boundary conditions

#### 4.1.2 Modelling of riser

The riser is modelled in Abaqus with data from the workover riser at the Gjøa field, provided by FMC Technologies. The given data is not sufficient to make an exact reproduction of the riser at Gjøa, hence some assumptions are needed. The given inner and outer diameters are used to model the strength of the pipe elements. In frequency analysis the mass is one of the crucial parameters and the mass of this riser is  $m = 214.38 \times 10^3 Kg$ . To get the correct mass of each section is the density determined, based on the inner and outer diameter and the length. Both Young's Modulus  $E_s = 201 GPa$  and Poisson's ratio  $\nu_s = 0.3$  are the same for all sections. The tension ring has been modelled as a point mass  $m_t = 9000 Kg$ . Added mass is applied on the submerged parts with a value of the added mass coefficient  $C_a = 1$ . The riser is meshed with 214 linear pipe elements (PIPE31H). One assumption when modelling with pipe elements is that each section must have the same diameter and the taper sections must be divided into 4-6 subsections with growing diameter. The bails has not been taken into account in this analysis.

#### 4.1.3 Boundary conditions

The riser is fully fixed at the seabed and a pinned boundary condition is applied at the top end; the riser is free to move in vertical direction. Vertical tension is applied at the bottom of the bails and at the tension ring, see Figure 19. The tension at the bottom of the bails and the tension ring are  $420 kN$  and  $1173 kN$ , respectively. One assumption is that horizontal spring supports at the bottom of the bails and at the tension ring is omitted. These strings were inserted in the original model to give a pendulum effect of the associated components.

#### 4.1.4 Currents at Gjøa field

A detailed investigation of currents at the Gjøa field was provided by Statoil and RiserTec and resulted in 22 different velocity profiles. Each velocity profile is given with an associated probability that they occur. High current levels are anticipated to dominate VIV fatigue, but the highest current levels are also the most infrequently. One difficult task is to find the most critical velocity profile which both has high probability to occur and high current velocity.

The current velocities are measured at eight different levels and the current profile is obtained by linear interpolation between this measurement points. Four of the velocity profiles are shown in Figure 20. Velocity profile number 1 is the most common with a probability to occur of 38.50%, but it is also the least harmful. Velocity profile number 10 and 19 has a probability to occur of 0.2% and 0.00014%. The most critical velocity profile is number 22 which has a probability to occur of 0.00003%, it corresponds to  $9s/year$ .

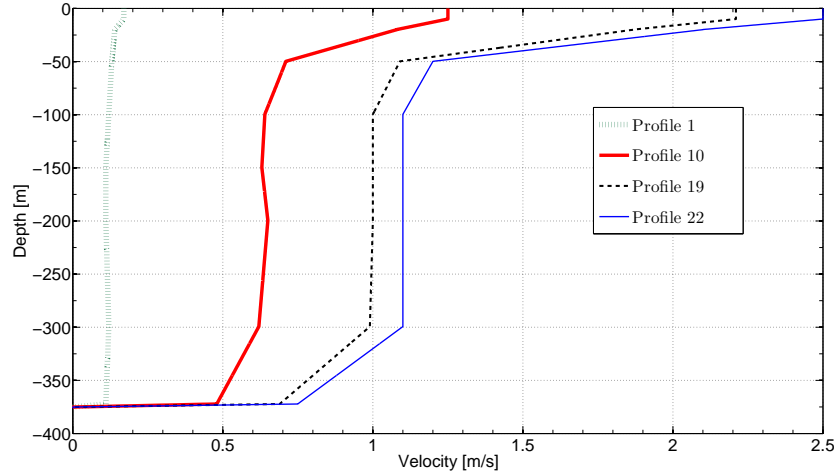


Figure 20: Velocity profiles

#### 4.1.5 Frequency analysis

In RiserTecs report on the workover riser in the Gjøa field, a frequency analysis of the riser is presented. RiserTec has used SHEAR7 for determination of the eigenfrequencies and if one can assume that the analysis is correctly executed, good correlation with the Abaqus analysis should be obtained. However, the details in RiserTecs report are not sufficient to expect a complete agreement. For more details about SHEAR7, see [49].

#### 4.1.6 VIV analysis

The input values for the CFD analysis on the short riser are given from the VIV analysis. In a looping procedure all velocity profiles are compared with all possible eigenfrequencies that can be excited and it results in reduced velocities for all diameters of the riser. The critical range of the reduced velocity is  $5 < V_r < 8$  see, Section 2.2.6. By studying how many element and which eigenmodes that are subjected to the critical reduced velocity, a critical diameter and a critical velocity can be selected.

### 4.2 Results riser analysis

The eigenfrequencies from the Abaqus analysis are compared with those from SHEAR7 and shown in Figure 21 and in Table 4. When computing the difference between the two approaches the SHEAR7 analysis has been used as reference.

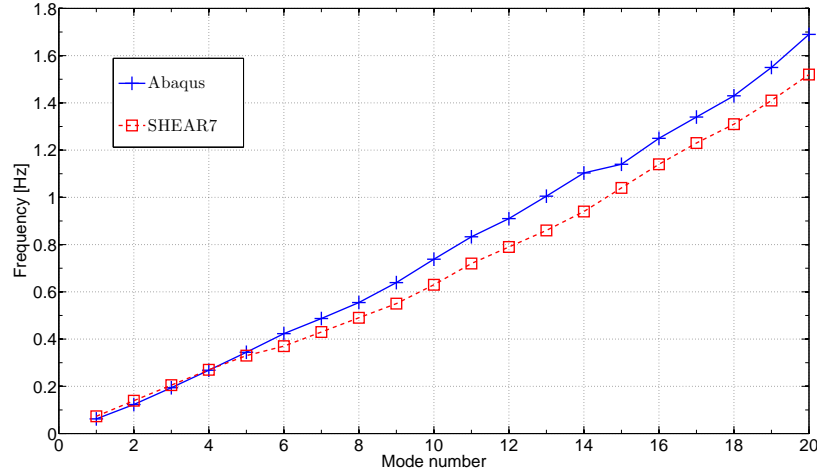


Figure 21: Eigenfrequencies for the Abaqus and SHEAR7 analysis

Table 4: Comparison of eigenfrequencies

	Mode 1	Mode 2	Mode 3	Mode 4	Mode 5	Mode 6	Mode7
Abaqus	0.062 Hz	0.123 Hz	0.194 Hz	0.268 Hz	0.344 Hz	0.423 Hz	0.487 Hz
Shear7	0.073 Hz	0.139 Hz	0.205 Hz	0.27 Hz	0.33 Hz	0.37 Hz	0.43 Hz
Diff	15%	11%	5.4%	0.74%	4.2%	14%	13%
	Mode 8	Mode 9	Mode 10	Mode 11	Mode 12	Mode 13	Mode 14
Abaqus	0.546 Hz	0.639 Hz	0.738 Hz	0.833 Hz	0.910 Hz	1.005 Hz	1.1033 Hz
Shear7	0.49 Hz	0.55 Hz	0.63 Hz	0.72 Hz	0.79 Hz	0.86 Hz	0.94 Hz
Diff	13%	16%	17%	15%	15%	17%	17%

As one can see in Table 4, there is a relatively large difference between the eigenfrequencies for the majority of the modes. From the 5:th mode and later, the eigenfrequencies are higher for the Abaqus model, which means that the VIV analysis based on the eigenfrequencies from the SHEAR7 model are more conservative than the Abaqus model.

By using the reduced velocity, the number of modes that are into the critical interval of reduced velocities can be determined. The analysis is performed for each velocity profile and it give information which the critical modes are. Figure 22 and Figure 23 are related to each other and Figure 22 show how many eigenmodes that excite more than 50% of the submerged riser and which of these modes that are the highest. The 12:th mode is the highest mode to excite more than 50% of the elements and it can be excited for the five highest velocity profiles. Four modes are the maximum number of modes that one velocity profile can excite. Figure 23 show almost the same thing, but shows more clearly that four modes (mode 9, 10, 11 and 12) are the most critical for velocity profile 22 and three modes (mode 6, 7 and 8) are the most critical for velocity profile 10.

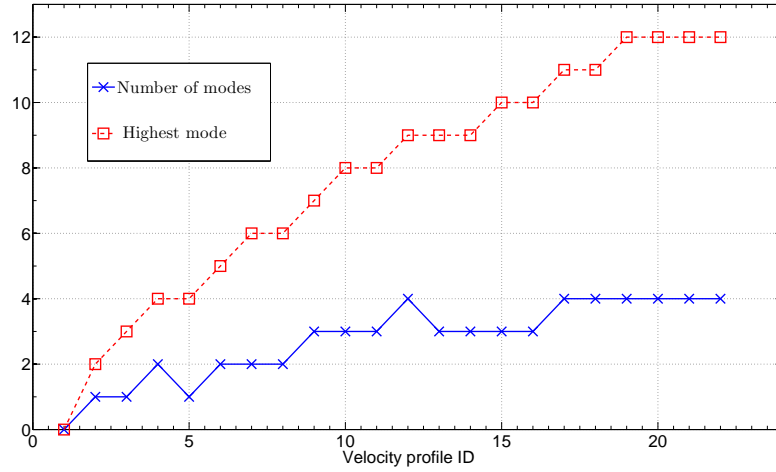


Figure 22: Highest possible mode and maximum number of modes to be excited

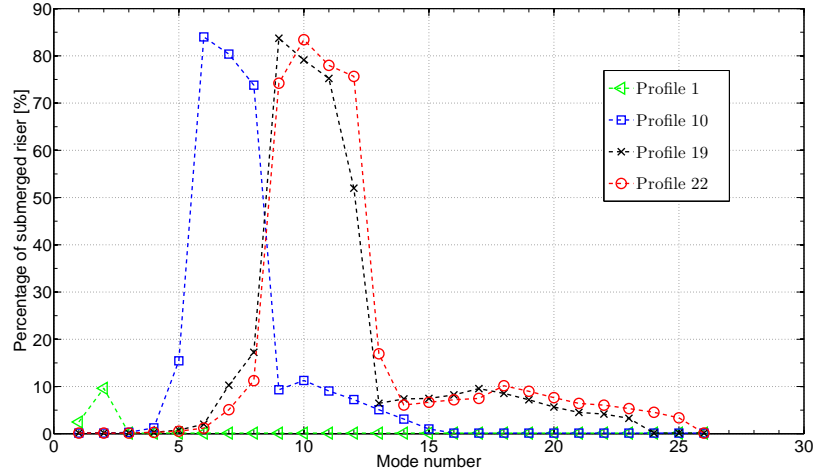


Figure 23: Percent of the submerged riser in critical range of reduced velocity

It is not possible to simulate all velocities and all diameters in this thesis and therefore only one interesting velocity with corresponding diameter will be selected and further evaluated. Velocity profile number 22 may excite four modes, with mode number 12 as the highest. The probability that the currents are so strong as they are for velocity profile 22 are on the other hand very low. Velocity profile 19 may also excite four modes, where the highest mode is number 12. The probability that velocity profile 19 will occur is almost five times higher than for velocity profile number 22. The velocity profile that has been chosen for further evaluation and is expected to be the most critical is number 19. Figure 24 show the reduced velocity for mode 5, 9 and 15 when velocity profile number 19 is applied. The critical velocities and diameters for mode 11 and velocity profile 19 are shown in Figure 25, where the critical reduced velocity is in the range  $5 < V_r < 8$ . It should be noted that these assumptions only are arbitrary.

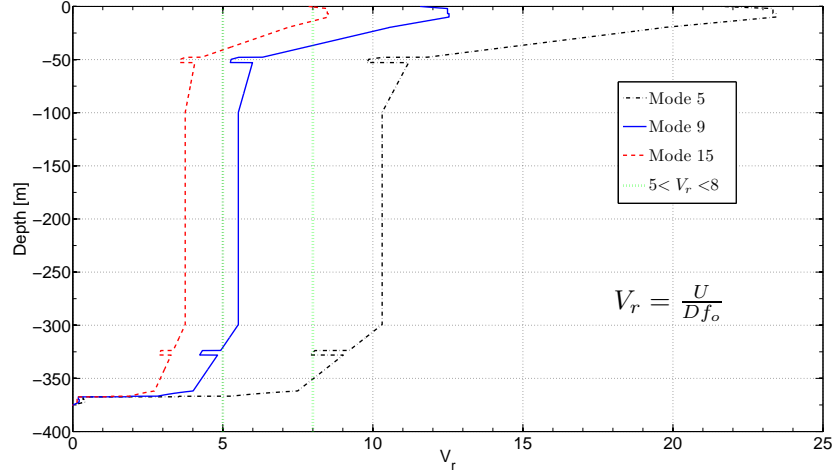
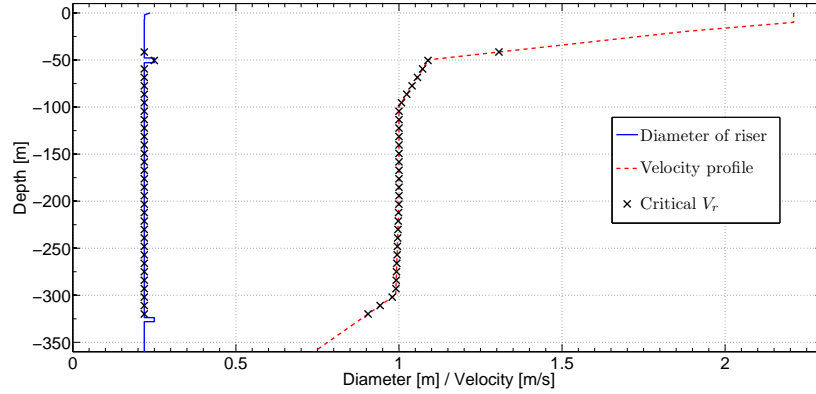


Figure 24: Reduced velocity along the submerged riser for velocity profile number 19

Figure 25: Diameters and velocities related to  $5 < V_r < 8$ 

### 4.3 Discussion riser analysis

The eigenfrequency analysis differ rather much from the SHEAR7 analysis and the 11:th eigenfrequency in the Abaqus analysis correspond to the 12:th in the SHEAR7 analysis. Influence of the spring supports and the extra mass from the bails will affect the result, but in which extent is hard to say. All details used in RiserTecs analysis is not clearly defined for example how the interior liquid is modelled. The frequencies are in a narrow span and the first 10 eigenfrequencies are within  $0.676Hz$ . However, the range  $5 < V_r < 8$  has been found to be the most critical in several previous experiments, but not in all. A change in the range of reduced velocity will also change the critical eigenfrequencies for the riser, and other modes and current velocities will be the most devastating. For a cross section with  $D = 0.2191m$  and a free stream velocity  $U = 1m/s$  the selected range for reduced velocities correspond to an eigenfrequency range for the riser of  $1.096Hz < f_o < 1.753Hz$ . It is far from obvious under which conditions VIV is expected to occur and as long as the results are approximately close to the experimental values the analysis becomes valuable. Another possible reason for deviations in the frequency analysis is that different beam models are used.

Figure 24 and Figure 25 show that the Dual Bore with  $D = 0.2191m$  is the most interesting section and the velocity in this region is  $U = 1m/s$ . The Dual Bore is by far the largest part of

the riser and it is very long and slender and of course the most vulnerable. This study is not sufficiently for a complete analysis of the riser. More than one mode will probably be excited at the same time, but it is difficult to anticipate when and for which conditions it would happen.

Based on Figure 22 and Figure 23 the 19:th velocity profile is founded to be the most critical, but it cannot be verified without experiments. However, the 19:th are still a critical velocity profile and even if worse condition can occur, it is relevant for VIV investigations.

## 5 CFD on short riser

Analysis of full-scale risers requires tremendous models and the computational time becomes very long. In this method study, analysis on a full-scale riser is not feasible and therefore a shorter section of the riser has been evaluated. Before an FSI analysis on a short riser can be performed, it is suitable to evaluate the flow around a fixed and rigid riser. The aim of a CFD study on a short riser is to find a fine mesh and an appropriate turbulence model that predict the physics of the flow.

### 5.1 Method CFD on short riser

Based on the recommendations from the riser analysis, see Section 4.3, the geometry for this CFD analysis is created. Three different meshes are evaluated and compared. The purpose with the different meshes is not to create the best possible mesh, rather to find an economical and fairly accurate mesh. The Reynolds number over the riser is high and turbulence must be solved. Three different methods to model the turbulence are evaluated and compared. The meshes and all simulations are completely performed in STAR-CCM+ and the investigated parameters are lift coefficient, drag coefficient and Strouhal number.

#### 5.1.1 Geometry and mesh

A principle sketch of the domain is shown in Figure 26. The Dual Bore with a diameter  $D = 0.2191m$  was found to be a good reference diameter for this short riser section, see Section 4.2. Based on the diameter of the riser section, a fluid domain has been created. The dimensions of the domain are  $9D$  upstream,  $27D$  downstream and  $7D$  in the directions perpendicular to the flow. The second decisive parameter is the ratio  $L/D$ . A ratio  $L/D = 20$  is chosen which result in a length of the riser of  $L = 4.382m$ . This domain should be large enough to capture 3D effects, without very computational expensive simulations. With a ratio  $L/D = 20$  it is also easy to compare the drag coefficient with experimental values.

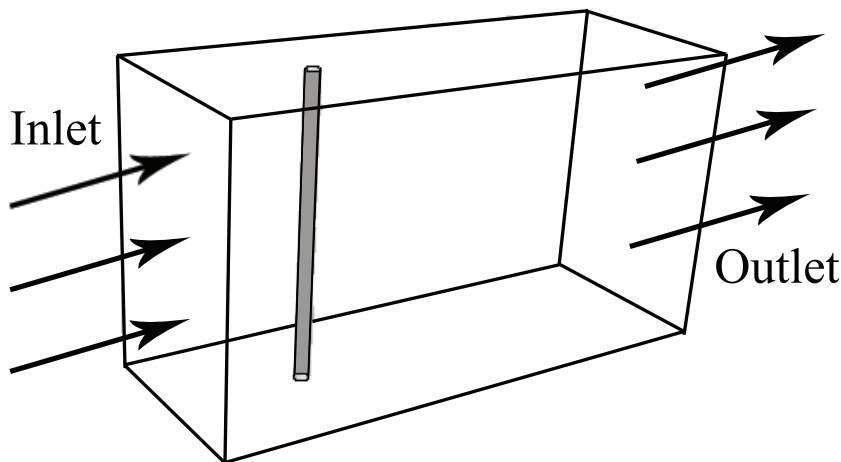


Figure 26: Fluid domain

One of the main tasks of this analysis is to study different meshes. From the knowledge that full-scale riser are very long and require enormous domains, it is important to know how coarse a



mesh can be, but still predict vortex shedding with sufficiently accuracy. Three meshes, all with hexahedral element and different grid sizes has been created in STAR-CCM+. The cells are isotropic and the cell sizes for the different blocks and meshes are given in Table 5. Each mesh is divided into three blocks, see Figure 27, which give opportunities to make refinements in interesting areas, such as the wake. Block 1 has the dimension  $3.5D \times 6.5D$  and Block 2  $8.5D \times 18.5D$ .

Table 5: Comparison of meshes

	Block 1	Block 2	Block 3	Number of cells
Mesh 1	19.0 [mm]	38.0 [mm]	74.6 [mm]	1353622
Mesh 2	12.5 [mm]	25.0 [mm]	50.0 [mm]	4135303
Mesh 3	7.50 [mm]	15.0 [mm]	60.0 [mm]	16440906

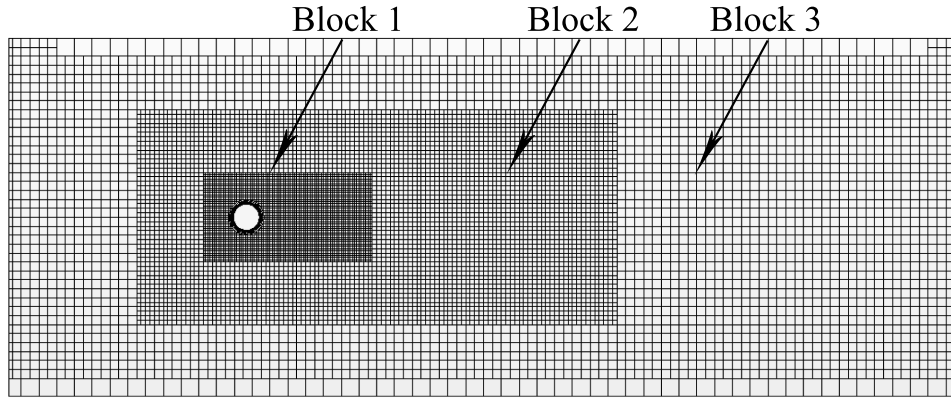


Figure 27: Mesh 1

A fine mesh resolution in the boundary layer is important to capture the physics. The most accurate approaches to model flows, such as Direct Numerical Simulation (DNS) and Large Eddy Simulation (LES) are too time-consuming for this application and turbulence models are used instead. The turbulence model and the wall treatment, see Section 5.1.1 govern how the near wall cells in the boundary layer should be designed. The same boundary layer resolution and wall treatment is used for all three meshes. 15 prism layers has been used and the height of the first cell  $\Delta x = 0.0001m$

### Wall treatment

One very important parameter in flows where the wall behavior must be well resolved, is the non-dimensional wall distance  $y^+$  [9]. In general should  $y^+ < 1$ , but reliable results can be achieved even if the  $y^+$  criteria not is fulfilled. Wall treatments are used to model the near wall behavior and STAR-CCM+ provide three types of wall treatments. The *High  $y^+$  wall treatment* implies a wall function approach in which it is assumed that the first cell in the prism layer lies in the logarithmic region of the boundary layer,  $y^+ > 30$ . The *Low  $y^+$  wall treatment* is suitable for low-Reynolds number turbulence models in which it is assumed that the viscous sublayer,  $y^+ < 5$ , is properly resolved. A third approach is a blended wall function called *All  $y^+$  wall treatment* which behave as the *Low  $y^+$  wall treatment* in regions with fine mesh and as *High  $y^+$  wall treatment* in regions where the mesh is coarser. The three wall treatments is evaluated for

model that use the coarse mesh, *Mesh 1* and *SST  $k - \omega$*  as turbulence model. By changing the size of the boundary layer cells, the different criteria for wall treatments are satisfied.

### Material properties

The purpose of this analysis is to model a riser section somewhere between  $100m$  and  $300m$  below sea surface. The fluid properties are chosen to approximately represent water at deep sea with density  $\rho_f = 1025 \frac{Kg}{m^3}$  and dynamic viscosity  $\mu_f = 0.0015 \frac{Ns}{m^2}$ .

### Boundary conditions and Solver set-up

The modelled riser section represents a part of the real riser that is located far away from the seabed and the water surface. Except for the inlet- and the outlet boundary, all other surrounding boundaries have been modelled with symmetry conditions. The properties of the solver are:

Table 6: Simulation settings and boundary conditions for flow past short riser

Settings	Choice
Temporal discretization	$2^{nd}$ order
Convection scheme	$2^{nd}$ order upwind
Turbulence model	Standard Spalart-Allmaras
Flow	Segregated
Time model	Implicit unsteady
Solver algorithm	SIMPLE
Time step	0.001s
Simulated time	20s
<i>Boundary conditions:</i>	
Riser	No-slip wall
Inlet	Velocity inlet
Outlet	Pressure outlet
Left boundary	Symmetry plane
Right boundary	Symmetry plane
Upper boundary	Symmetry plane
Lower boundary	Symmetry plane

A free stream velocity  $U = 1m/s$  and a diameter on the riser  $D = 0.2191m$  correspond to a Reynolds number  $Re = 1.5 \times 10^5$ . A Reynolds number of  $Re = 1.5 \cdot 10^5$  is fairly high and the vortices are unsteady, see Figure 4. Flow around circular cylinders at high Reynolds number is quite well documented and data from these experiments are compared with results from the short riser analysis.

## 5.2 Results CFD on short riser

This result chapter is divided into three parts. The first section presents the lift coefficient for the three different turbulence models and the three different meshes. The second part is similar to the first section, but with focus on the drag coefficient. The last section is about wall treatments and how these affect the drag- and lift coefficient.

### 5.2.1 Lift coefficient

The lift coefficient for the coarse mesh, *Mesh 1* are presented in Figure 28. Figure 29 and Figure 30 show the results for the medium mesh, *Mesh 2* and the fine mesh, *Mesh 3* respectively.

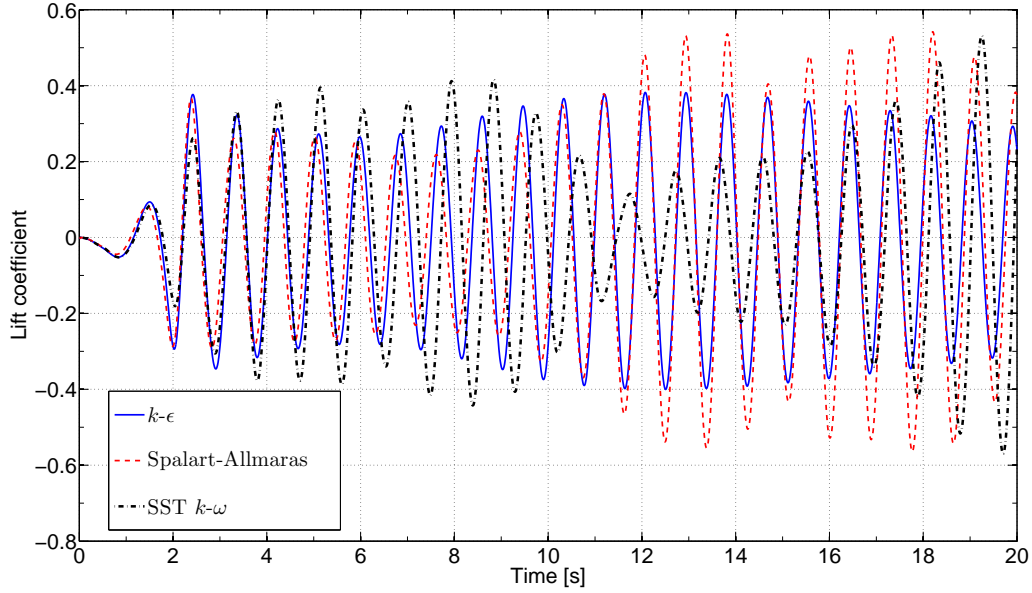


Figure 28: Lift coefficient for the coarse mesh, *Mesh 1*

When studying the shedding frequency for *Mesh 1*, one can see that the  $k - \epsilon$  model and the *Spalart-Allmaras* model are almost identical, whilst the *SST k -  $\omega$*  model has a slightly lower shedding frequency. The amplitude of the lift coefficient is fairly unsteady for the *SST k -  $\omega$*  model and a significant drop in the amplitude can be seen at  $t = 10s$ . Opposite to *SST k -  $\omega$*  model, the *Spalart-Allmaras* model exhibit an increase of the amplitude at  $t = 10s$  and reach it maximum,  $C_L = 0.55$  at  $t = 13.8s$ . The  $k - \epsilon$  model is very steady around an amplitude of  $C_L = \pm 0.4$

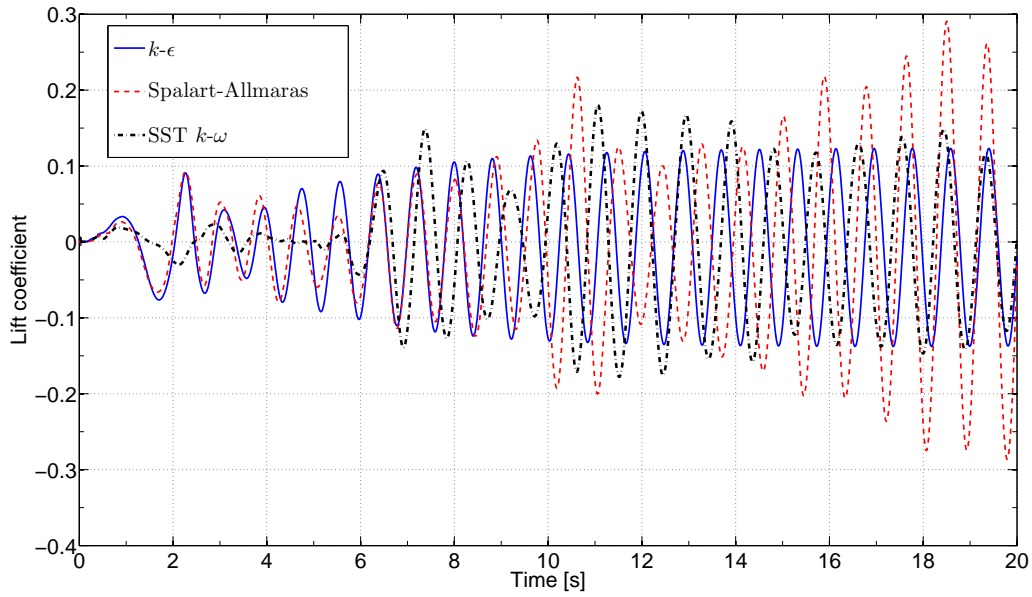
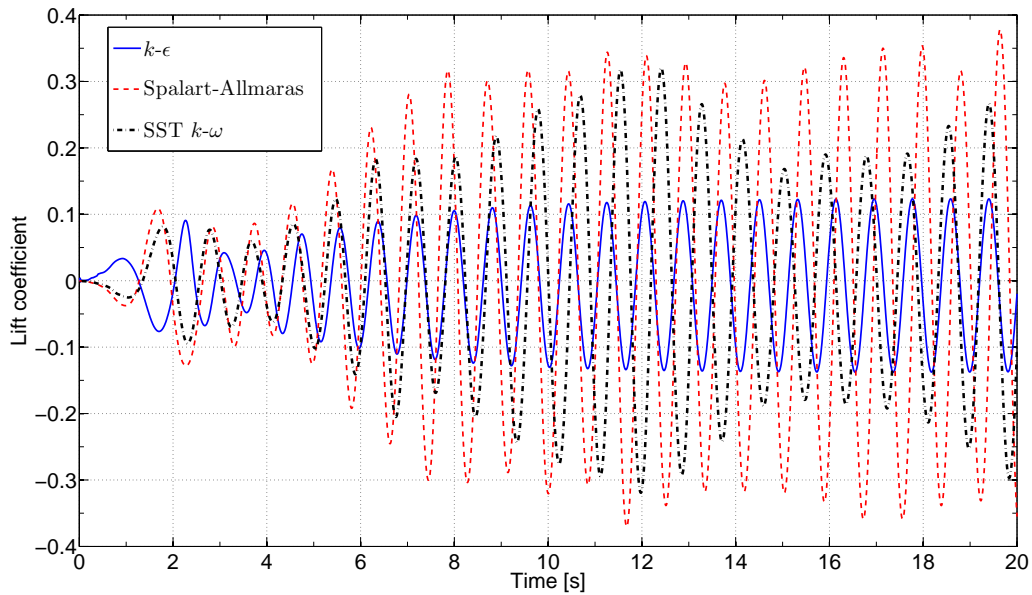
Figure 29: Lift coefficient for the medium mesh, *Mesh 2*

Figure 29 shows that the magnitude of the oscillations are fairly equal for the three models, but only half of the magnitude compared to the coarse mesh. Notable is that the *SST k -  $\omega$*  model start to oscillate very late compare to the other models and the other mesh qualities.

Figure 30: Lift coefficient for the fine mesh, *Mesh 3*

The finest mesh should be the most accurate, but in this case does at least the lift coefficient for *Mesh 3* not behave as expected. The *k -  $\epsilon$*  model follow a clear pattern with decreasing magnitude of the lift coefficient when the mesh is refined. The *Spalart-Allmaras* model and the *SST k -  $\omega$*  model for *Mesh 3* are somewhere in between the coarse mesh and the medium mesh.

Figure 31 show the variation of the lift coefficient for the *SST k -  $\omega$*  model for the different

meshes. The amplitude for *Mesh 1* are larger than for *Mesh 2* and *Mesh 3* until  $t = 10s$ .

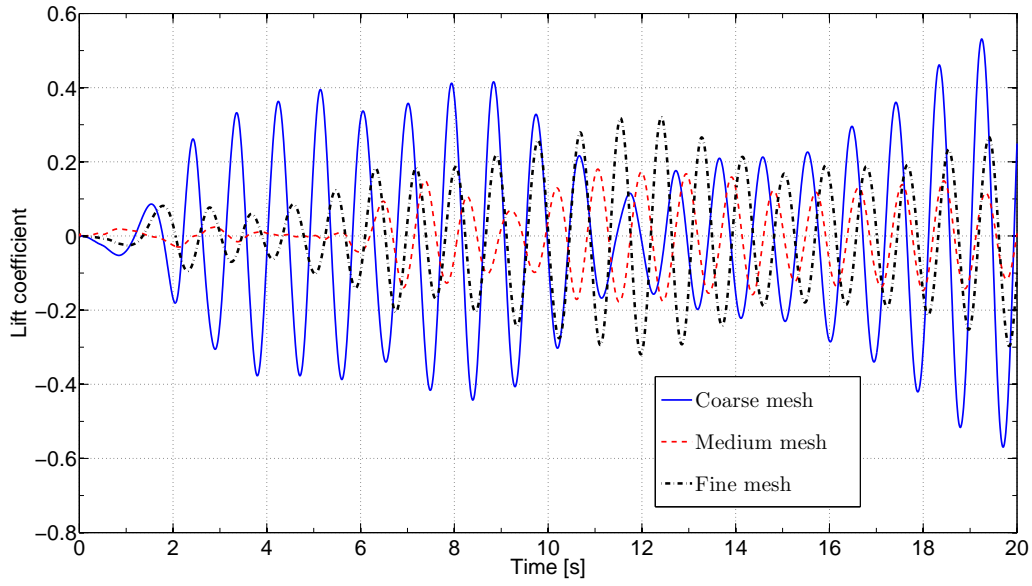


Figure 31: Lift coefficient for the  $SST\ k - \omega$  model

### 5.2.2 Drag coefficient

The drag coefficient is presented in the same manner as the lift coefficient. According to [21], a ratio  $L/D = 20$ , should correspond to a drag coefficient  $C_D = 0.91$ .

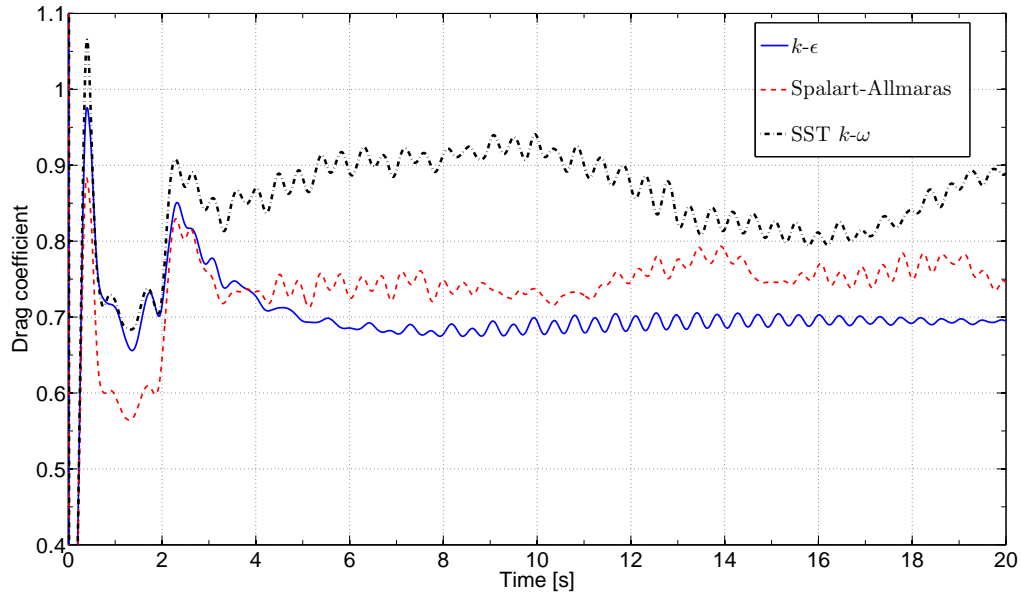
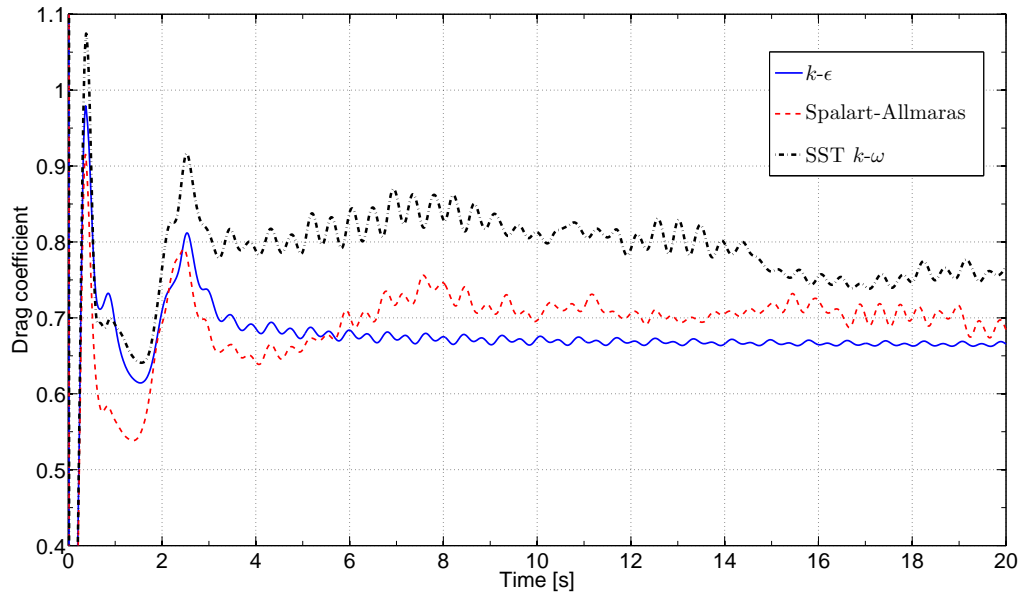
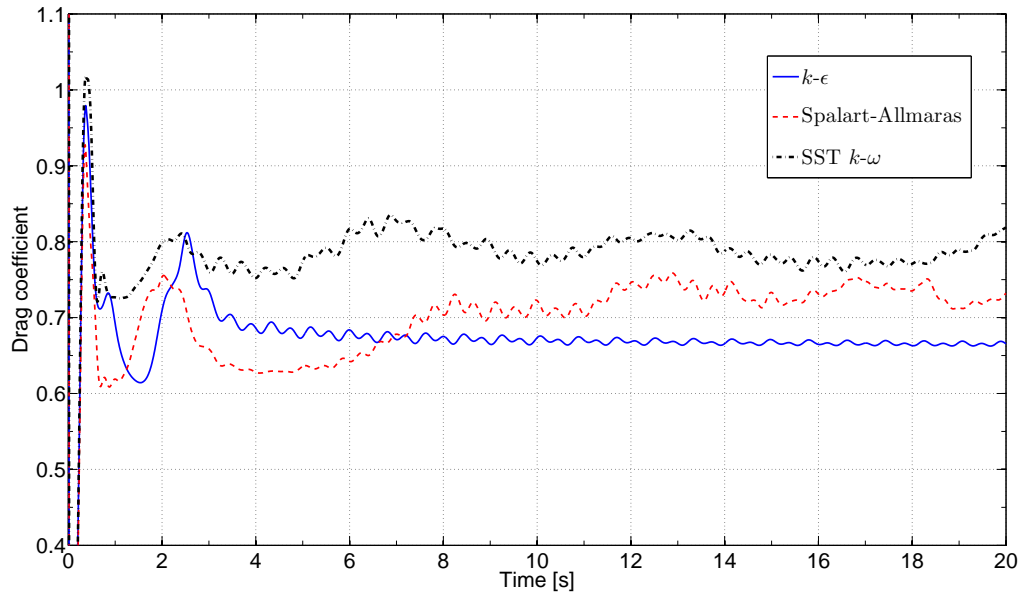
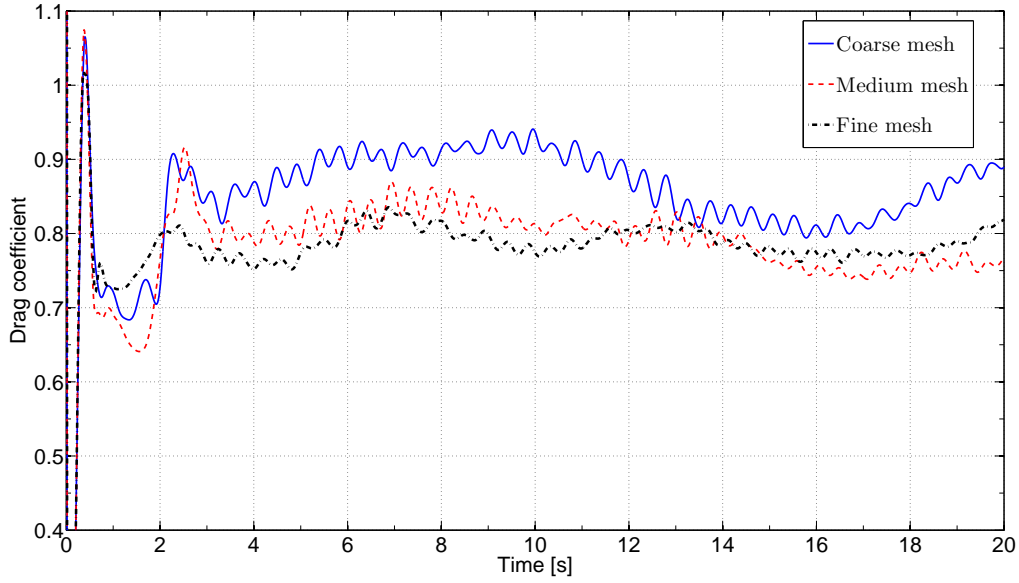


Figure 32: Drag coefficient for the coarse mesh, *Mesh 1*

Independent of mesh, the largest value for the drag coefficient is obtained with the  $SST\ k - \omega$  model, followed by the *Spalart-Allmaras* model. In the time interval  $5 < t < 12$  and at  $t = 20$  the drag coefficient for  $SST\ k - \omega$  model with *Mesh 1* is very close to 0.9.

Figure 33: Drag coefficient for the medium mesh, *Mesh 2*Figure 34: Drag coefficient for the fine mesh, *Mesh 3*

The drag coefficient behave more as expected than the lift coefficient and no large deviations between the meshes are shown. The largest values of the drag coefficient are obtained with *Mesh 1*. The magnitude of the drag coefficient are lower for *Mesh 2* and *Mesh 3* but not in large extent and it seems that it starts to converge.

Figure 35: Drag coefficient for the  $SST k - \omega$  model

The Strouhal number are correlated to the Reynolds number and  $Re \approx 1.5 \times 10^5$  correspond to  $St \approx 0.20$ . A summary of the results from the CFD simulations are presented in Table 7. The r.m.s values of the lift coefficient and the drag coefficient are measured in the interval  $4 < t < 20$ .

Table 7: Compilation of results

Mesh	$k - \epsilon$			SST $k - \omega$			Spalart-Allmaras		
	$C'_{L,rms}$	$C_{D,rms}$	St	$C'_{L,rms}$	$C_{D,rms}$	St	$C'_{L,rms}$	$C_{D,rms}$	St
Mesh 1	0.33	0.69	0.25	0.32	0.87	0.24	0.38	0.75	0.25
Mesh 2	0.11	0.67	0.27	0.13	0.79	0.24	0.15	0.70	0.25
Mesh 3	0.11	0.67	0.28	0.23	0.79	0.25	0.3	0.71	0.26

Except for *Mesh 1* the drag coefficient is under predicted, particular for the  $k - \epsilon$  model. The Strouhal number for all meshes and turbulence models are in the interval  $0.25 < St < 0.28$ , which is slightly higher than the reference value. Notable is that the Strouhal number increase with finer mesh and deviates more from the reference value. The  $SST k - \omega$  model is closer to this reference values both in terms of drag coefficient and Strouhal number. The shedding frequency for *Mesh 1* with the  $SST k - \omega$  model is  $f_s = 1.09Hz$ .

### 5.2.3 Near wall treatment

Three different wall treatment approaches is evaluated in this study. The reference value is *Mesh 1* with the  $SST k - \omega$  model as turbulence model, see Figure 31 and Figure 35. With a *High  $y^+$  wall treatment* is the resulting  $y^+ > 30$  at a major part of the riser, but locally  $y^+ \approx 15$ . The  $y^+$  value when the *Low  $y^+$  wall treatment* is applied is  $y^+ < 0.54$ . The lift and drag forces are shown in Figure 36 and Figure 37 and the deviations from the model with *All  $y^+$  wall treatment* where  $3 < y^+ < 63$ , are significant.

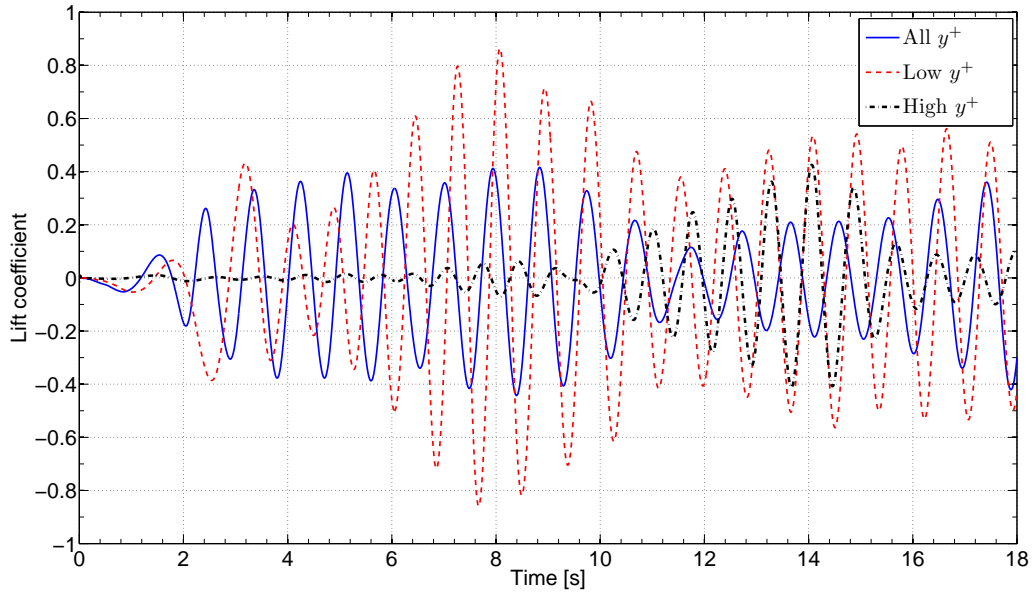


Figure 36: Variation of lift coefficient with different wall treatments

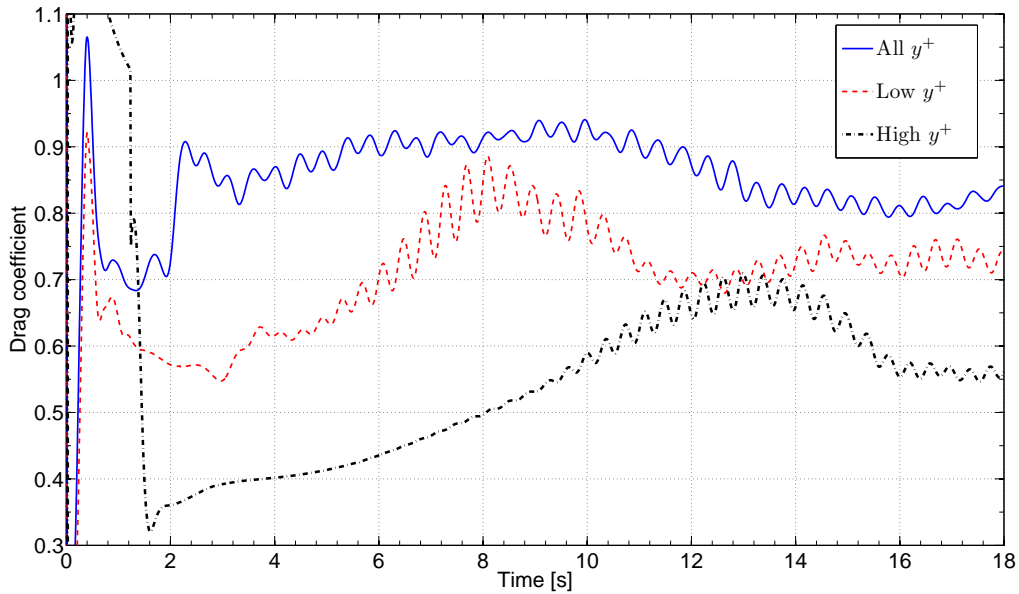


Figure 37: Variation of drag coefficient with different wall treatments

### 5.3 Discussion CFD on short riser

The mesh quality is probable the most decisive parameter in CFD simulations. The evaluated meshes in this thesis are not appropriate for more detailed studies. However, the purpose of the thesis is to find a method for simulating VIV in large scale risers. Hence, very good mesh resolution are not applicable.

Using a block structure for this application is appropriate, but a more optimized design is preferable. The size of the blocks is not investigated in detail and *Block2* is probably larger



than required. The shape of the block is not either optimized and a block with conical shape should be more suitable. It is also desirable to have one block with slowly growing cell sizes instead of a couple of blocks with different grid size.

Another critical issue is how the flow should be solved. In this thesis, turbulence models are used to model the turbulent flow, but turbulence models are just only models of reality. How accurate a model is for one specific flow case, depends on several parameters and the model should be verified with experiments under same conditions. Assumptions according to the mesh and turbulence model makes that it is not expected that the results in this analysis comply fully with experiments.

The *SST  $k - \omega$*  model is, not unexpected, closer to the experimental values for drag coefficient and Strouhal number than the other turbulence models. The lift coefficient is more difficult to compare since the experimental values are more difficult to interpret. The lift coefficient for the *SST  $k - \omega$*  model and the *Spalart - Allmaras* model is fairly unsteady and further refinements of the mesh is necessary to obtain convergence. The  *$k - \epsilon$*  model follow a more clear pattern for all evaluated parameters, but it is also the model with worst the performance.

Three different types of wall treatments have been evaluated. Figure 36 and Figure 37 show large differences between the models. The *Low  $y^+$  wall treatment* has very fine mesh resolution in the near wall cells and a  $y^+$  well below 1. The  $y^+$  for the *High  $y^+$  wall treatment* is a bit too small at a minor part of the riser surface but in general well above 30. Wall treatments have shown to be tricky and *All  $y^+$  wall treatment* should be used in most cases.

## 6 Fluid-Structure Interaction on riser

Solving FSI problems with structures undergoing large deformations, such as the flag in *Turek&Hron's* benchmark, see Section 3, include several challenging issues. How to obtain a steady solution for these kinds of problem is not obvious. A large part of this thesis has been related to stability parameters in the coupling procedure. Before the coupling procedure can be studied, each field must be analyzed separately to obtain stable solutions without any interaction. When starting to interact between the fields, experience from the separate analysis can be useless since the prevailing conditions for fields in motion may be totally different. Two risers, *Model 1* and *Model 2* with different structural properties has been studied.

### 6.1 Method Fluid-Structure Interaction on short riser

#### 6.1.1 Geometry and mesh

The fluid domain for this FSI analysis is the same as in Section 5.1.1 and the fluid mesh is, based on recommendations in Section 5.3, the same as the coarse mesh, *Mesh 1*. The riser is modelled in Abaqus with 3975 quadratic, second-order, thick shell elements, S8R. For more details about S8R, see [43]. The circumferential mesh density has shown to be important in FSI analysis, although the solvers can handle a small gap between the interface surfaces. The riser has been modelled with 25 elements in circumferential direction, but fewer elements may be preferable to reduce the computational time. Since the coupling frequency is high, the structure will be solved many times within each time step and a cheap structural mesh is important. Shell elements are easy to implement in FSI analysis since the coupling surface is clearly defined. The structural mesh is shown below.

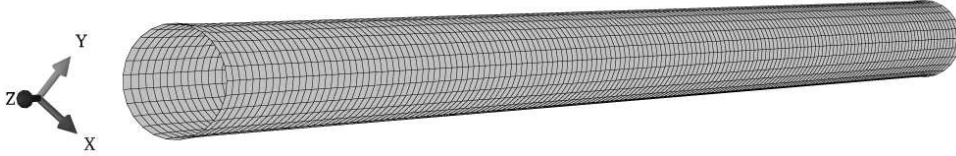


Figure 38: The meshed riser

#### Material properties

The properties for the fluid is, as in Section 5.1.1 water with density  $\rho_f = 1025 \frac{Kg}{m^3}$  and dynamic viscosity  $\mu_f = 0.0015 \frac{Ns}{m^2}$ . The real riser is mainly made of steel and has low eigenfrequencies, see Section 4.2 and the eigenfrequencies are related to the length and the stiffness of the riser. In this analysis, only a short section is studied and the same stiffness cannot be used to obtain the same eigenfrequencies as for the full scale riser. The span of eigenfrequency, interesting in a VIV point of view is stated in Section 4.3 and based on these data, the short riser is modelled. The density and Poisson's ratio of the riser is the same as steel, namely  $\rho_s = 7800 \frac{Kg}{m^3}$  and  $\nu_s = 0.3$ . The main assumption with this material model is Young's modulus, which has been reduced significant, more than thousand times smaller than steel to a value of  $E_s = 120MPa$  for *Model 1* and  $E_s = 160MPa$  for *Model 2*. The first eigenfrequency for the short riser with *Model 1* is  $1.22Hz$ , which correspond to a reduced velocity of  $V_r = 5.56$ . The first eigenfrequency for the short riser with *Model 2* is  $1.39Hz$ , which correspond to a reduced velocity of  $V_r = 6.36$ . A Raleigh damping with  $\alpha = 0.0028$  and  $\beta = 0.0014$  is introduced in the structure and the total mass of the riser section is  $m = 485.82Kg$ .

### Boundary conditions and Solver set-up

Many of the settings for this analysis is the same as used in previous sections, but the time step has been reduced to get stability in the coupling.

Table 8: Simulation settings and boundary conditions for FSI on short riser

Settings	Choice
Temporal discretization	2 <sup>nd</sup> order
Convection scheme	2 <sup>nd</sup> order upwind
Turbulence model	SST $k - \omega$
Flow	Segregated
Time model	Implicit unsteady
Solver algorithm	SIMPLE
Time step	0.0007s
<i>Boundary conditions:</i>	
<i>Fluid domain:</i>	
Riser	No-slip wall
Inlet	Velocity inlet
Outlet	Pressure outlet
Left boundary	Symmetry plane
Right boundary	Symmetry plane
Upper boundary	Symmetry plane
Lower boundary	Symmetry plane
<i>Structure:</i>	
Lower end (z=-4.382m)	Pinned
Upper end (z=0)	$\delta_x = 0, \delta_y = 0$

To avoid buckling and stabilize the riser, tension at the upper end is applied. The magnitude of the top tension is  $T = 400N$  for both *Model 1* and *Model 2*. The tension has small effect on the elongation of the riser, but give support so it not deform by its own weight.

The stability in the coupling depends on a number of parameters. Three important parameters to obtain more stable solutions are described below.

- Large peaks of the pressure and the shear stress, which are exported to Abaqus, can be devastating and lead to rapid divergence. A clipping parameter has been introduced to reduce peaks of the exported values.
- The time step has been reduced to  $\Delta t = 0.0007s$ , since larger time steps have shown to give diverging solutions.
- Making the fluid slightly compressible has shown to be an effective method to obtain more stable solutions, see Section 3.4.

The FSI simulation is performed in a fully developed flow. Hence, the first six seconds in the analysis is simulated with fixed and rigid cylinder.

## 6.2 Results Fluid-Structure Interaction on short riser

This model has not much lower stiffness and the ratio  $L/D$  is much smaller than for real risers. Hence, comparison with existing models is not feasible and no clear conclusions can be drawn. The most important with these results is to see if the physics behave in accordance with the theory.

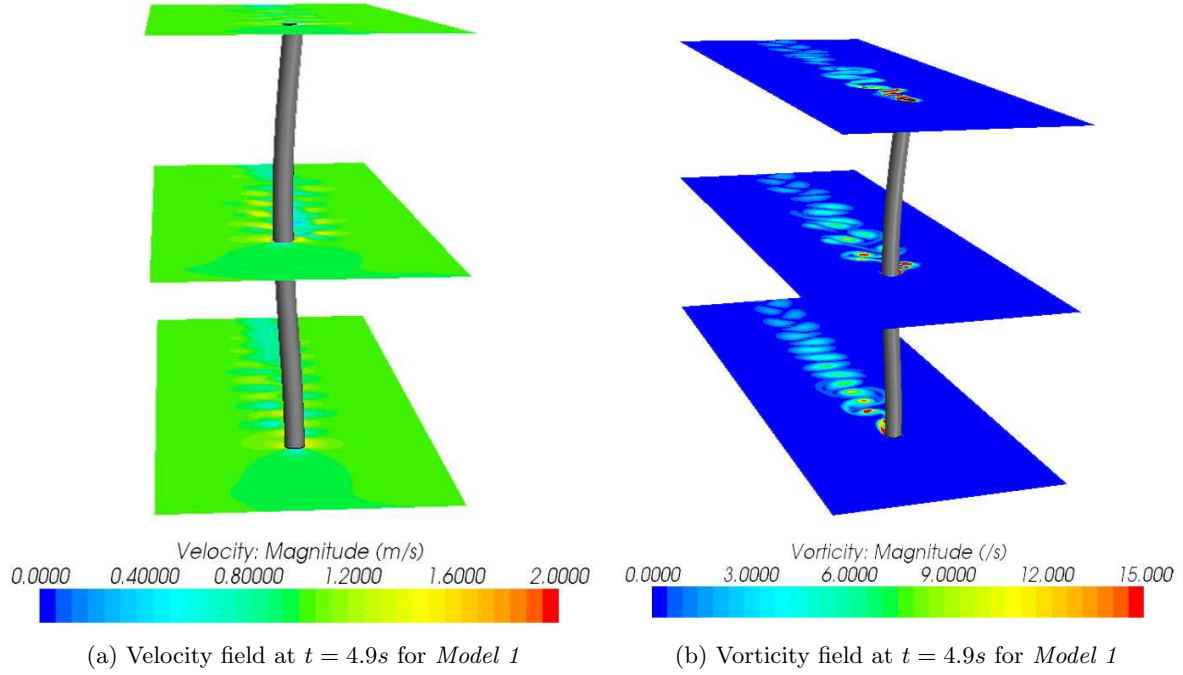


Figure 39: Velocity and vorticity field at  $z = 0m$ ,  $z = 2.5m$  and  $z = 4.382m$

Figure 39a show the velocity field and the deformed riser at the last time step of the simulation  $t \approx 4.9s$ . The riser is free to move in vertical direction at the top end, see Table 8. Therefore, the deformation of the riser is largest slightly above the  $z/2$  and the control point at  $z = 2.5$  is chosen as reference point.

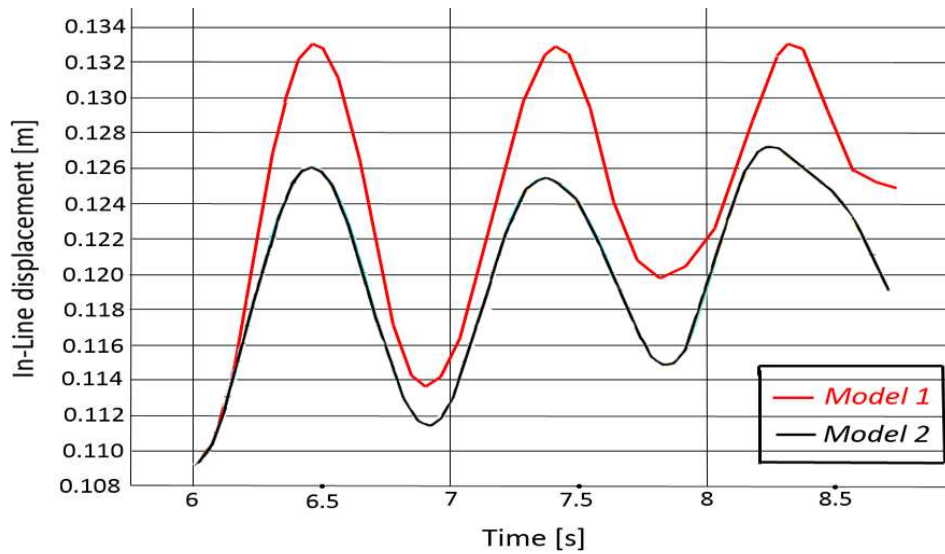


Figure 40: The In-line displacement for *Model 1* and *Model 2* at  $z = 2.5$

As one can see in Figure 40, the In-Line displacement for *Model 2* is smaller than for *Model 1*. Only a few oscillations has been simulated and no critical displacements has been developed yet. In this early state, a smaller displacement is expected for *Model 2*, since the model is stiffer than *Model 1*. However, the forces on *Model 2* are larger and it may result in more critical conditions after a while, see Figure 41.

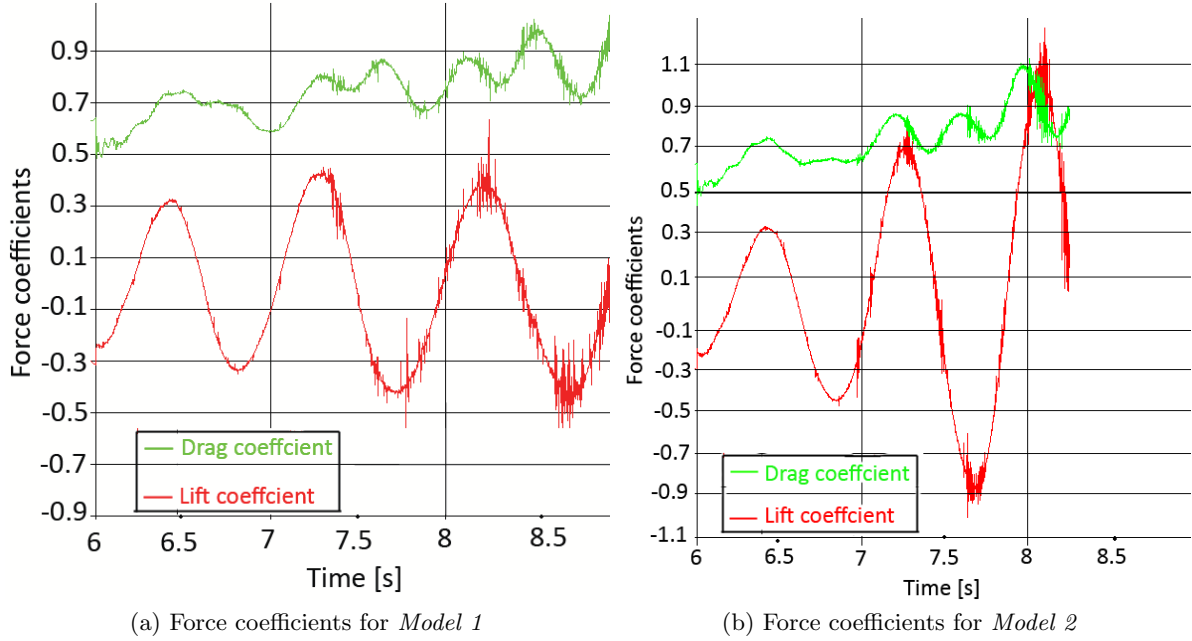


Figure 41: Force coefficients for *Model 1* and *Model 2*

A further analysis of *Model 2* is not possible due to the time limit of the thesis. Hence, the following results are only from *Model 1*. The displacement in x-direction, the In-line displacement is much smaller than the Cross-flow displacement. As described in Section 2.2.6, the Cross-flow displacement should be much larger than the In-line displacement, but the difference in amplitude is larger than expected. The amplitude of the Cross-flow displacement increases in a clear manner and the maximal displacement within the simulated time correspond to a value of  $A/D = 0.62$ . However, the amplitude is still growing and the maximum value of  $A/D$  is not obtained. The period of the oscillations is  $\delta t = 0.88s$ , which correspond to a frequency of  $f_v = 1.14Hz$ .

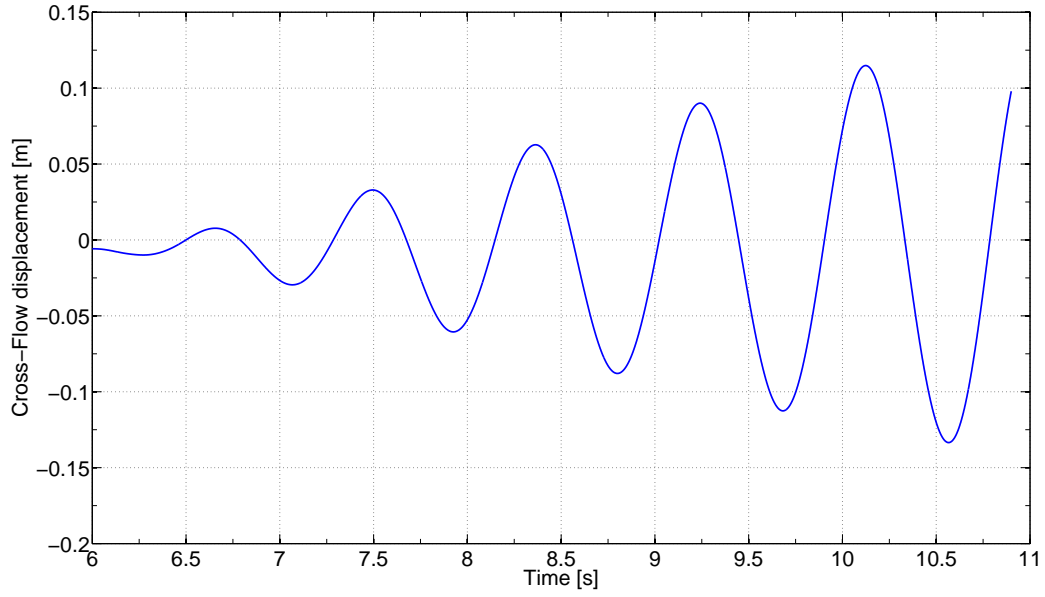


Figure 42: The Cross-Flow displacement at  $z = 2.5\text{m}$  for *Model 1*

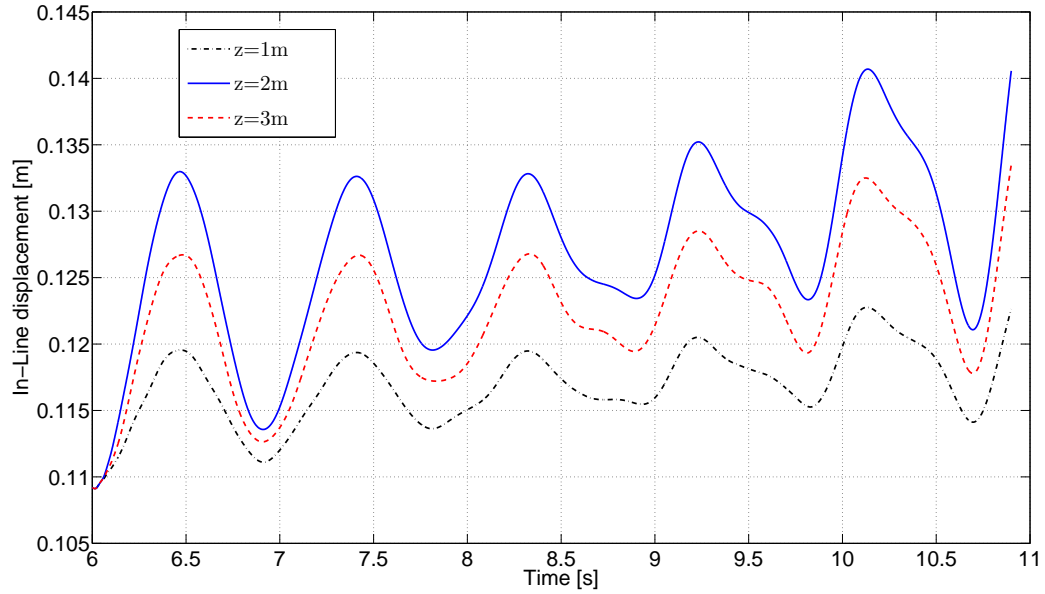


Figure 43: The In-Line displacement at  $z = 1.5\text{m}$ ,  $z = 2.5\text{m}$  and  $z = 3.5\text{m}$  for *Model 1*

The In-Line displacement is more unsteady than the Cross-Flow displacement and does not follow a smooth curve. This is particular evident at  $8.5 < t < 9.8$  but similar behavior has been obtained for other riser analysis, see [10]. The shifting In-Line displacement makes that the motion of the riser becomes somewhat strange.

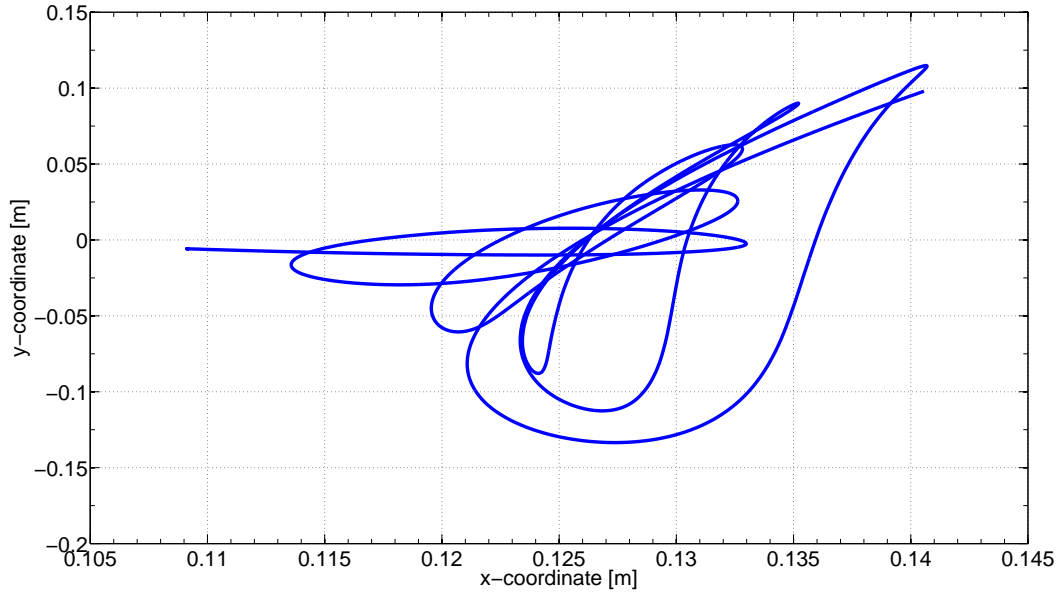


Figure 44: The motion in the x-y plane at  $z = 2.5m$  for *Model 1*

During the first two seconds after the FSI simulation started ( $6s < t < 8s$ ), the drag coefficient are unsteady. After  $t = 8s$ , both the drag and lift coefficient increase in a clear manner and the oscillation frequency for the drag is two times the oscillation frequency for the lift, in accordance with the theory.

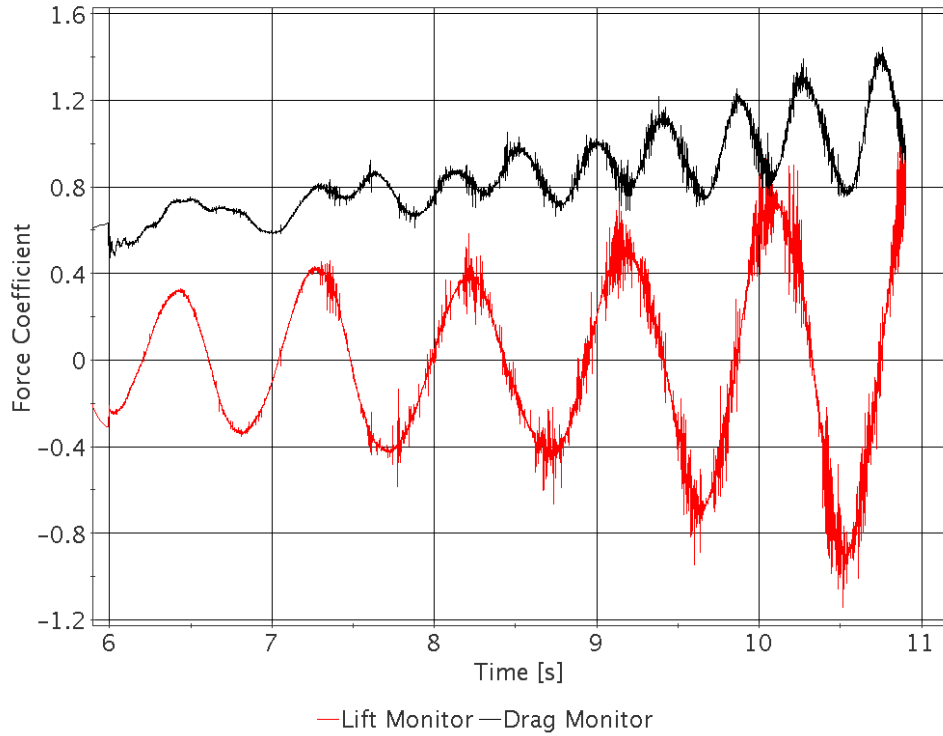


Figure 45: Force coefficients for *Model 1*

### 6.3 Discussion Fluid-Structure Interaction on Riser

The computational time, using 22 cpus for a fixed riser is  $\delta t = 28.8s$  for one time step with 20 inner iterations. The computational time for one iteration is approximately 1.4s. The coupling procedure is very time-consuming and it is desirable to use as few coupling iterations as possible. The computational time for one time step for the fully coupled riser section with 18 cpus for STAR-CCM+ and 6 cpus for Abaqus, 20 inner iterations and 12 coupling iterations is 125s. The time it takes for one coupling iteration is then approximately 8s, more than 5.5 times longer than for a pure CFD iteration. The required time for each structural iteration varying as well as the required coupling iterations. To make this method commercial for larger models, the settings in the structural solver must be evaluated.

The short riser is much stiffer than the flag in the benchmark and the Co-simulation displacement converges faster for the short riser. 20 inner iterations are definitely sufficient for both these models, but for more flexible structures, a larger number of coupling iterations is required. The fluid converges within 20 inner iterations so with a more flexible structure it is suitable to introduce a new stopping criterion so that both the number of inner iterations and Co-simulation convergence are satisfied.

The simulated time should be longer to ensure that the solution converge and nothing unexpected occurs. More analysis with different conditions of both the fluid and the structure should be performed to make an overall analysis. It is interesting to see if it is possible to simulate higher modes. Abaqus 6.12 does not support a Co-simulation coupling with STAR-CCM+ using pipe elements in an easy way. Use of pipe elements are preferred in a time-consuming perspective and it is appropriate to get this coupling to work so existing riser models based on pipe-elements easy can be implemented.

The mesh used for the FSI simulation is the coarsest of the three evaluated meshes, *Mesh 1*. However, since no convergence is obtained from the mesh study and no turbulence model predict the reference value very well, *Mesh 1* is a reasonable choice. The FSI simulation in this thesis should be compared with one that uses a mesh that predicts the reference values better. Comparison with experimental values and results from a simulation based on empirical models, such as SHEAR7 is necessary to verify the model.



## 7 Concluding remarks

A method to simulate VIV on risers has been developed and the model behaves in a reasonable way. The solution of the model is stable and somewhat conservative, hence not very efficient and reduction of computational time is important. The method must be verified before any proper conclusions can be drawn. Flows with different Reynolds number should be evaluated to get a more clear view of the method. The most interesting test case is to reduce the stiffness of the structure and see if the method is able to simulate higher-order eigenmodes.

Two-way FSI is a very challenging field in engineering analysis and a carefully selected time step is one of the most important parameter regarding FSI. In pure CFD simulations, the time step must be sufficiently low to predict the flow accurate. In FSI simulations, especially in cases with significant motion of the structure, the solution tends to diverge if the time step is too large. The time step equal to the one used in pure CFD simulation is in general sufficient for an FSI simulation, but slightly smaller time step is preferable to avoid failures. A small time step smooths out large oscillations and the results become more accurate.

The computational time is a crucial parameter when planning FSI analysis related to risers since the computational domain is very large. Optimization of the fluid mesh is particularly important and refinements in the mesh should be used with afterthought. Refining the mesh very much is not realizable since only small refinements of the mesh in the block structure increase the total number of cells dramatically. The results from the mesh study in Section 5 is difficult to interpret since the results not converge clearly. Hence, further evaluations of the fluid mesh are recommended.

In the FSI analysis of the riser, the coarsest mesh, *Mesh 1* has been used. However, the most time-consuming part of the FSI analysis performed in this thesis is solving the structural equations in Abaqus and the coupling procedure itself. The computational time for the FSI simulation is significantly larger compared to pure the CFD simulations with same mesh. The largest focus in this thesis has been related to CFD, but it has been shown that the cheap structural solution is very important and this should be studied further. An iterative coupling algorithm is necessary. Therefore, optimization of the required number of coupling iterations within each time step is very important. The optimization should be time dependent since the prevailing conditions change a lot during a complete simulation, as well as the required number of coupling iterations. One way to do this is to exchange data at every second time step and introduce a stopping parameter that require convergence in the Co-simulation before advancing in time.

Shell elements are used for modelling the riser and only one grid is studied. A coarser mesh will surely not affect the solution in a negative sense. Shell elements is rather computationally expensive and use of pipe elements will reduce the computational time significant. Unfortunately, Abaqus 6.12 does not support this coupling with STAR-CCM+ but this approach should be studied further for later versions of Abaqus.



## References

- [1] Wikipedia [Internet]. *Deepwater Horizon oil spill*. [cited 2012 Oct 23]. [http://www.wikipedia.org/wiki/Deepwater\\_Horizon\\_oil\\_spill](http://www.wikipedia.org/wiki/Deepwater_Horizon_oil_spill).
- [2] Wikipedia [Internet]. *Oil platform*. [cited 2012 Oct 11]. [en.wikipedia.org/wiki/Oil\\_platform](http://en.wikipedia.org/wiki/Oil_platform).
- [3] Statoil [Internet]. *Brochure*. [cited 2012 Oct 15]. <http://www.statoil.com/en/ouoperations/explorationprod/partneroperatedfields/gjoea>.
- [4] Anatol Roshko. On the development of turbulent wakes from vortex streets. *NACA Rep.1191*, 1954.
- [5] Anatol Roshko. Experiments on the flow past a circular cylinder at very high reynolds number. *Journal of Fluid Mechanics/Volume 10 / Issue 03 / May 1961, pp 345-356*, 1961.
- [6] Jr. Samuel Holmes, Owen H. Oakley and Yiannis Constantinides. Simulation of riser viv using fully three dimensional cfd simulations. *OMAE-92124*, 2006.
- [7] Chia-Rong Chen Hamn-Ching Chen, Kevin Huang and Richard S. Mercier. Cfd simulation of a riser viv. *Prepared for the Minerals Management Service Under the MMS/OTRC Cooperative Research Agreement 1435-01-04-CA-35515 Task Orders 35983 and 39774 MMS Project Number 481*, 2007.
- [8] Kjell Randa Kjell Herfjord, Tore Holmås. A parallel approach for numerical solution of vortex induced vibrations of very long risers. *COMPUTATIONAL MECHANICS, New Trends and Applications, S. Idelsohn, E.Oñate. E Dvorkin (Eds.) ©CIMNE, Barcelona, Spain 1998*, 1998.
- [9] CD-adapco. *User Guide, STAR-CCM+ Version 7.04.006*.
- [10] Jr. Farzin Shakib Rajeev K. Jaiman, Owen H. Oakley and Yiannis Constantinides. Fully coupled fluid-structure interaction for offshore applications. *OMAE2009-79804*, 2009.
- [11] J. Cebal O. Soto, R. Lhner and R. Codina. A time-accurate implicit-monolithic finite element scheme for incompressible flow problems. *Proc. ECCOMAS CFD*, 2001.
- [12] E.H. van Brummelen R. de Borst C. Michler, S.J. Hulshoff. A monolithic approach to fluid-structure interaction. *Computers & Fluids Volume 33, Issue 5-6, June-July 2004, Pages 839-848*, 2003.
- [13] Robby Haelterman Jan Vierendeels Joris Degroote, Peter Bruggeman. Stability of a coupling technique for partitioned solvers in fsi applications. *Computers & Structures Volume 86, Issues 23-24, December 2008, Pages 2224-2234*, 2008.
- [14] Ekkehard Ramm Christiane Förster, Wolfgang A. Wall. Artificial added mass instabilities in sequential staggered coupling of nonlinear structures and incompressible viscous flows. *Computer Methods in Applied Mechanics and Enginerring, Volume 196, Issue 7, 10 January 2007, Pages 1278-1293*, 2006.
- [15] Jean-Frdric Gerbeau Paola Causin and Fabio Nobile. Added-mass effect in the design of partitioned algorithms for fluid-structure problems. *Computer Methods in Applied Mechanics and Enginerring, Volume 194, Issues 42-44, 15 October 2005, Pages 4506-4527*, 2004.

- [16] Kristoffer G. van der Zee Charbel Farhat and Philippe Geuzaine. Provably second-order time-accurate loosely-coupled solution algorithms for transient nonlinear computational aeroelasticity. *Computer Methods in Applied Mechanics and Engineering, Volume 195, Issues 17-18, 15 March 2006, Pages 1973-2001.*
- [17] Eric Loth Rajeev Jaiman, Philippe Geubelle and Xiangmin M. Jiao. Stable and accurate loosely-coupled scheme for unsteady fluid-structure interaction. *AIAA Paper, 07-334*, 2007.
- [18] Pavel Vachal Milan Kucharik, Richard Liska and Mikhail Shashkov. Arbitrary lagrangian-eulerian (ALE) methods in compressible fluid dynamics. *Programs and Algorithms of Numerical Mathematics 13, Pages 178-183*, 2006.
- [19] J.-Ph. Ponthot Jean Donea, Antonio Huerta and A. Rodriguez-Ferran. Arbitrary lagrangian-eulerian methods. *Encyclopedia of Computational Mechanics*, 2004.
- [20] Dr. S. M Fielding. Laminar boundary layer theory, 2005. Lecture notes Durham University.
- [21] Frank M. White. *Fluid Mechanics Sixth edition*. McGraw-Hill, 2008.
- [22] Lars Davidsson. *Fluid mechanics, turbulent flow and turbulence modeling*. cited 2012 Sep 3. [http://www.tfd.chalmers.se/~lada/comp\\_turb\\_model/lecture\\_notes.html](http://www.tfd.chalmers.se/~lada/comp_turb_model/lecture_notes.html).
- [23] CFD Online [Internet]. *Introduction to turbulence/Wall bounded turbulent flows*.
- [24] Langley Research Center [Internet] NASA. *The Spalart-Allmaras Turbulence Model*. cited 2012 Oct 11. [turbmodels.larc.nasa.gov/spalart.html](http://turbmodels.larc.nasa.gov/spalart.html).
- [25] Fluent Inc. *User Guide, FLUENT 6.1*.
- [26] F. R. Menter. Two-equation eddy-viscosity turbulence models for engineering applications. *AIAA-Journal*, 32(8), pp. 269-289.
- [27] Qiang Bai Yong Bai. *Subsea pipelines and risers*. Elsevier.
- [28] Neil Willis Paolo Simantiras. Investigation on vortex induced oscillations and helical strakes effectiveness at very high incidence angles. *Proceedings of the International Offshore and Polar Engineering Conference, Brest, France, 1999*.
- [29] Halvor Liea Gro Sagli Baarholma, Carl Martin Larsen. Reduction of viv using suppression devices an empirical approach. *Marine Structures, Volume 18, Issues 7-8, September-November 2005, Pages 489-510*.
- [30] Sheldon I. Green. *Fluid Vortices: Fluid Mechanics and its applications*. Kluwer Academic Publishers, 1995.
- [31] John H. Lienhard. *Synopsis of Lift, Drag, and Vortex Frequency Data for Rigid Circular Cylinders*. Technical Extension Service, Washington State University, 1966.
- [32] Hugh Blackburn and Ron Henderson. Lock-in behaviour in simulated vortex-induced vibration. *Experimental Thermal and Fluid Science, Volume 12, Issue 2, February 1996, Pages 184-189*.
- [33] Muhammad Reza Gharib. *Vortex-Induced Vibration, Absence of Lock-in and Fluid Force Deduction*. Phd thesis, California Institute of Technology, Source DAI-B 62/04, p. 1922, Oct 2001, 182 pages, 1999.
- [34] C.H.K. Williamson and R. Godvardhan. Vortex-induced vibrations. *Annual Review of Fluid MEchanics, Volume 36, January 2004, Pages 413-455*, 2004.

- [35] Martin Søreide. Experimental investigation of in-line and cross-flow viv. *Proceedings of The Thiteenth (2003) International Offshore and Polar Engineering Conference, Honolulu, Hawaii*, 2003.
- [36] Det Norske Veritas. Environmental conditions and environmental loads. *Recommended Practice, DNV-RP-C205, October 2010*.
- [37] Marian Wiercigroch Narakorn Srinil and Patrick O’ Brien. Reduced-order modelling of vortex-induced vibration of catenary riser. *Ocean Engineering, Volume 36, Issues 17-18, Pages 1404-1414*, 2009.
- [38] Steve Perryman Radboud van Dijk, Allan Magee and Joe Gebara. Model test experience on vortex induced vibrations of truss spars. *Offshore Technology Conference, 5 May-8 May 2003, Houston, Texas*, 2003.
- [39] Vivek Jaiswal Vikas Jhingran and J. Kim Vandiver. Spatial variation of drag on long cylinders in sheared flow. *Proceedings of the 27th International Conference on Offshore Mechanics and Artic Engineering, OMAE2008-57803*, 2008.
- [40] Anne Marthine Rustad. *Modeling and Control of Top Tensioned Risers*. Doctoral thesis, Norwegian University of Science Technology, 2007.
- [41] Andrew J. Kurdila Roy R. Craig. *Fundamentals of Structural Dynamics*. John Wiley & Sons, Inc, 2006.
- [42] Stefan Turek and Jaroslav Hron. Proposal for numerical benchmarking of fluid-structure interaction between an elastic object and laminar incompressible flow. *Fluid-Structure Interaction, Lecture Notes Computational Science and Engineering, Volume 53, 2006, Pages 371-385*.
- [43] SIMULIA. *Abaqus Theory Manual 6.11*.
- [44] AcuSim [Internet]. [cited 2012 Oct 15]. <http://www.acusim.com>.
- [45] Inc. Altair Engineering. *AcuSolve V1.8b Release Notes*.
- [46] CD adapco [Internet]. [cited 2012 Oct 18]. <http://www.cd-adapco.com>.
- [47] Brian Donning, 2012.
- [48] M Razzaq H. Wobker M Schfer S. Turek, J Hron. Numerical benchmarking of fluid-structure interaction: A comparison of different discretization and solution approaches. *Fluid-Structure Interaction II, Lecture Notes Computational Science and Engineering, Volume 73, 2010, Pages 413-424*.
- [49] J.Kim Vandiver and Li Li. *SHEAR7 V4.4 program theoretical manual*.

